

## THE LICK AGN MONITORING PROJECT: BROAD-LINE REGION RADII AND BLACK HOLE MASSES FROM REVERBERATION MAPPING OF $H\beta$

MISTY C. BENTZ<sup>1,16</sup>, JONELLE L. WALSH<sup>1</sup>, AARON J. BARTH<sup>1</sup>, NAIRN BALIBER<sup>2,3</sup>, VARDHA NICOLA BENNETT<sup>2,4</sup>,  
GABRIELA CANALIZO<sup>4,5</sup>, ALEXEI V. FILIPPENKO<sup>6</sup>, MOHAN GANESHALINGAM<sup>6</sup>, ELINOR L. GATES<sup>7</sup>, JENNY E. GREENE<sup>2,8</sup>,  
MARTON G. HIDAS<sup>2,3,9</sup>, KYLE D. HINER<sup>4,5</sup>, NICHOLAS LEE<sup>6</sup>, WEIDONG LI<sup>6</sup>, MATTHEW A. MALKAN<sup>10</sup>, TAKEO MINEZAKI<sup>11</sup>,  
YU SAKATA<sup>11,12</sup>, FRANK J. D. SERDUKE<sup>6</sup>, JEFFREY M. SILVERMAN<sup>6</sup>, THEA N. STEELE<sup>6</sup>, DANIEL STERN<sup>13</sup>, RACHEL A. STREET<sup>2,3</sup>,  
CAROL E. THORNTON<sup>1</sup>, TOMMASO TREU<sup>2,17</sup>, XIAOFENG WANG<sup>6,14</sup>, JONG-HAK WOO<sup>10,15,16</sup>, AND YUZURU YOSHII<sup>11</sup>

<sup>1</sup> Department of Physics and Astronomy, 4129 Frederick Reines Hall, University of California, Irvine, CA 92697, USA; mbentz@uci.edu

<sup>2</sup> Physics Department, University of California, Santa Barbara, CA 93106, USA

<sup>3</sup> Las Cumbres Observatory Global Telescope, 6740 Cortona Dr. Ste. 102, Goleta, CA 93117, USA

<sup>4</sup> Institute of Geophysics and Planetary Physics, University of California, Riverside, CA 92521, USA

<sup>5</sup> Department of Physics and Astronomy, University of California, Riverside, CA 92521, USA

<sup>6</sup> Department of Astronomy, University of California, Berkeley, CA 94720-3411, USA

<sup>7</sup> Lick Observatory, P.O. Box 85, Mount Hamilton, CA 95140, USA

<sup>8</sup> Princeton University Observatory, Princeton, NJ 08544, USA

<sup>9</sup> School of Physics A28, University of Sydney, NSW 2006, Australia

<sup>10</sup> Department of Physics and Astronomy, University of California, Los Angeles, CA 90024, USA

<sup>11</sup> Institute of Astronomy, School of Science, University of Tokyo, 2-21-1 Osawa, Mitaka, Tokyo 181-0015, Japan

<sup>12</sup> Department of Astronomy, School of Science, University of Tokyo, 7-3-1 Hongo, Bunkyo-ku, Tokyo 113-0033, Japan

<sup>13</sup> Jet Propulsion Laboratory, California Institute of Technology, MS 169-527, 4800 Oak Grove Drive, Pasadena, CA 91109, USA

<sup>14</sup> Physics Department and Tsinghua Center for Astrophysics (THCA), Tsinghua University, Beijing, 100084, China

<sup>15</sup> Astronomy Program, Department of Physics and Astronomy, Seoul National University, Gwanak-gu, Seoul 151-742, Korea

Received 2009 June 24; accepted 2009 September 18; published 2009 October 8

### ABSTRACT

We have recently completed a 64-night spectroscopic monitoring campaign at the Lick Observatory 3-m Shane telescope with the aim of measuring the masses of the black holes in 12 nearby ( $z < 0.05$ ) Seyfert 1 galaxies with expected masses in the range  $\sim 10^6$ – $10^7 M_\odot$  and also the well-studied nearby active galactic nucleus (AGN) NGC 5548. Nine of the objects in the sample (including NGC 5548) showed optical variability of sufficient strength during the monitoring campaign to allow for a time lag to be measured between the continuum fluctuations and the response to these fluctuations in the broad  $H\beta$  emission. We present here the light curves for all the objects in this sample and the subsequent  $H\beta$  time lags for the nine objects where these measurements were possible. The  $H\beta$  lag time is directly related to the size of the broad-line region (BLR) in AGNs, and by combining the  $H\beta$  lag time with the measured width of the  $H\beta$  emission line in the variable part of the spectrum, we determine the virial mass of the central supermassive black hole in these nine AGNs. The absolute calibration of the black hole masses is based on the normalization derived by Onken et al., which brings the masses determined by reverberation mapping into agreement with the local  $M_{\text{BH}}-\sigma_*$  relationship for quiescent galaxies. We also examine the time lag response as a function of velocity across the  $H\beta$  line profile for six of the AGNs. The analysis of four leads to rather ambiguous results with relatively flat time lags as a function of velocity. However, SBS 1116+583A exhibits a symmetric time lag response around the line center reminiscent of simple models for circularly orbiting BLR clouds, and Arp 151 shows an asymmetric profile that is most easily explained by a simple gravitational infall model. Further investigation will be necessary to fully understand the constraints placed on the physical models of the BLR by the velocity-resolved response in these objects.

**Key words:** galaxies: active – galaxies: nuclei – galaxies: Seyfert

**Online-only material:** color figures

### 1. INTRODUCTION

Active galactic nuclei (AGNs) have long been known to vary in luminosity on timescales of years to months or even days (Matthews & Sandage 1963; Smith & Hoffleit 1963). Variability has played a central role in AGN studies. Combining the physical size constraints set by rapid variability with the high luminosities of AGNs led to the original argument that AGNs are powered by accretion onto supermassive black holes (Zel'dovich & Novikov 1964; Salpeter 1964). Variability is used as a reliable method for detecting AGNs in surveys (e.g., van

den Bergh et al. 1973; Heckman 1976; Véron & Hawkins 1995), and it is the fundamental basis upon which rests the technique of measuring black hole masses known as reverberation mapping (Blandford & McKee 1982; Peterson 1993).

Reverberation mapping is the most successful method employed for measuring the mass of the central black hole in broad emission-line AGNs. Rather than relying on spatially resolved observations, as do most studies of black holes in nearby quiescent galaxies, reverberation mapping resolves the influence of the black hole in the time domain through spectroscopic monitoring of the continuum flux variability and the delayed response, or “echo,” in the broad emission-line flux. The time lag between these changes,  $\tau$ , depends on the light-travel time across the broad-line region (BLR) and is on the order of light

<sup>16</sup> Hubble Fellow

<sup>17</sup> Sloan Fellow and Packard Fellow

days for nearby Seyfert galaxies, corresponding to spatial scales of  $\sim 0.001$  pc. Combining the radius of the BLR,  $c\tau$ , with the velocity width,  $v$ , of the broad emission line gives the virial mass of the central black hole via the simple gravitational relation  $M = c\tau v^2/G$  (neglecting a factor of order unity).

To date, successful reverberation-mapping studies have been carried out for approximately 36 active galaxies (compiled by Peterson et al. 2004, 2005 with additions by Bentz et al. 2006b, 2007; Denney et al. 2006, 2009; and Grier et al. 2008). One of the most important results to come from reverberation mapping is the detection of a correlation between the BLR radius and the luminosity of the AGN, the  $R_{\text{BLR}}-L$  relationship (Koratkar & Gaskell 1991; Kaspi et al. 2000, 2005; Bentz et al. 2006a, 2009a). Combining the  $R_{\text{BLR}}-L$  relationship with the simple virial mass equation results in an extremely powerful tool for estimating black hole masses in broad-lined AGNs from a single epoch of spectroscopy and two simple spectral measurements: the velocity width of a broad emission line, and the continuum luminosity as a proxy for the radius of the BLR. The  $R_{\text{BLR}}-L$  relationship is therefore fundamental to all secondary techniques used to estimate black hole masses in AGNs (e.g., Laor 1998; Wandel et al. 1999; McLure & Jarvis 2002; Vestergaard & Peterson 2006), and as such, current studies of black holes in AGNs rest upon the calibration provided by the reverberation-mapping sample (e.g., Onken et al. 2004; Collin et al. 2006; McGill et al. 2008).

The vast majority of reverberation experiments have investigated black holes with masses in the range  $10^7-10^9 M_\odot$ . Studies of lower mass black holes have largely been restricted by the lower luminosities associated with smaller AGNs, and the few studies that have been carried out have large measurement uncertainties. It is particularly important to have the correct calibration for AGNs in the mass range of  $10^6-10^7 M_\odot$ , as they are at the peak of the local black hole mass distribution function (e.g., Greene & Ho 2007). In particular, AGNs in this mass range may provide strong constraints on the mass accretion history of the Universe through the coupling of the central black hole and the host galaxy, as evidenced by the relationship between black hole mass and bulge luminosity (the  $M_{\text{BH}}-L_{\text{bulge}}$  relationship; e.g., Magorrian et al. 1998; Marconi & Hunt 2003; Bentz et al. 2009b) and the relationship between black hole mass and bulge stellar velocity dispersion (the  $M_{\text{BH}}-\sigma_*$  relationship; Ferrarese & Merritt 2000; Gebhardt et al. 2000; Tremaine et al. 2002).

With the goal of extending the range of masses probed by reverberation studies, we have carried out a 64-night spectroscopic monitoring campaign with the Lick Observatory 3-m Shane telescope, targeting AGNs having expected black hole masses in the range  $\sim 10^6-10^7 M_\odot$ . We report here the  $H\beta$  light curves and reverberation analysis for the entire sample of 13 AGNs included in the Lick AGN Monitoring Project (LAMP). For those objects with significant correlations between the  $H\beta$  and continuum light curves, of which there were nine, we quantify the time lag between the variations in the light curves and present the derived black hole masses. We also investigate the time lag behavior as a function of velocity across the  $H\beta$  line profile for six of the AGNs. We have previously published the  $H\beta$  results for one of the objects, Arp 151 (Mrk 40; Bentz et al. 2008, hereafter Paper I), and here we give an update to the results for Arp 151 based on slight modifications to the data processing, to be consistent with all the results presented here. The small changes to the measured time lag and derived black hole mass for Arp 151 are not significant.

**Table 1**  
Object List

Object	$\alpha_{2000}$ (hr min sec)	$\delta_{2000}$ ( $^\circ$ ' '')	$z$	$A_B^a$ (mag)	Alternate Name
Mrk 142	10 25 31.3	+51 40 35	0.04494	0.069	PG 1022+519
SBS 1116+583A	11 18 57.7	+58 03 24	0.02787	0.050	
Arp 151	11 25 36.2	+54 22 57	0.02109	0.059	Mrk 40
Mrk 1310	12 01 14.3	-03 40 41	0.01941	0.133	
Mrk 202	12 17 55.0	+58 39 35	0.02102	0.087	
NGC 4253	12 18 26.5	+29 48 46	0.01293	0.084	Mrk 766
NGC 4748	12 52 12.4	-13 24 53	0.01463	0.223	
IC 4218	13 17 03.4	-02 15 41	0.01933	0.132	
MCG -06-30-15	13 35 53.8	-34 17 44	0.00775	0.266	ESO 383-G035
NGC 5548	14 17 59.5	+25 08 12	0.01718	0.088	
Mrk 290	15 35 52.3	+57 54 09	0.02958	0.065	PG 1543+580
IC 1198	16 08 36.4	+12 19 51	0.03366	0.236	Mrk 871
NGC 6814	19 42 40.6	-10 19 25	0.00521	0.790	

**Note.** <sup>a</sup> The Galactic extinction is based on Schlegel et al. (1998).

## 2. OBSERVATIONS

Details of the target selection and the photometric monitoring campaign are presented by Walsh et al. (2009, hereafter Paper II). In short, the sample of AGNs chosen for this study is listed in Table 1 and is comprised of 12 nearby ( $z < 0.05$ ) AGNs with estimated black hole masses (based on single-epoch spectroscopy) in the range  $\sim 10^6-10^7 M_\odot$ , expected  $H\beta$  lags between 5 and 20 days, and relatively strong broad-line components to their  $H\beta$  lines. Also included as a “control object” is NGC 5548, which has 14 years of previous reverberation-mapping data and a well-determined black hole mass of  $6.54^{+0.26}_{-0.25} \times 10^7 M_\odot$  (Bentz et al. 2007 and references therein). Inclusion of NGC 5548 adds extra value to our sample by allowing a direct comparison of our results with those of previous reverberation-mapping experiments.

### 2.1. Photometry

Broad-band Johnson  $B$  and  $V$  monitoring of all 13 AGNs in the sample was carried out at four telescopes: the 30-inch robotic Katzman Automatic Imaging Telescope (KAIT), the 2-m Multicolor Active Galactic Nuclei Monitoring telescope (Yoshii 2002; Yoshii et al. 2003), the Palomar 60-inch telescope, and the 32-inch Tenagra II telescope. The details of the photometric monitoring are described in Paper II, but we include a summary here.

Each of the four telescopes was responsible for monitoring a subset of the sample. Biweekly observations of the targets began in early 2008 February, but was increased to nightly monitoring beginning the evening of 2008 March 17 (UT, both here and throughout), about one week before the spectroscopic monitoring began on 2008 March 25. The photometric light curves mainly follow variations in the continuum flux, and the response of the broad emission lines is delayed relative to changes in the continuum. By starting the photometric monitoring early, we hoped to ensure that all events at the beginning of the spectroscopic light curves would have associated events in the photometric light curves.

The images were reduced following standard techniques. The fluxes of the AGNs were measured through circular apertures as described in Paper II and differential photometry was obtained relative to stars within the fields, which themselves were calibrated to Landolt (1992) standard stars. A simple model of

**Table 2**  
Observation Log

Object	P.A. ( $^{\circ}$ )	$t_{\text{exp}}$ (s)	S/N <sup>a</sup>	Sec $z^b$
Mrk 142	90	$2 \times 900$	90	1.06
SBS 1116+583A	90	$2 \times 1200$	80	1.11
Arp 151	90	$2 \times 600$	80	1.10
Mrk 1310	90	$2 \times 900$	60	1.34
Mrk 202	180	$2 \times 900$	100	1.24
NGC 4253	60	$2 \times 450$	120	1.30
NGC 4748	180	$2 \times 450$	120	1.59
IC 4218	45	$2 \times 900$	100	1.45
MCG -06-30-15	180	$2 \times 900$	80	3.15
NGC 5548	60	$2 \times 300$	110	1.17
Mrk 290	90	$2 \times 450$	110	1.10
IC 1198	45	$2 \times 1200$	160	1.17
NGC 6814	150	$2 \times 900$	200	1.63

**Notes.**<sup>a</sup> The typical signal-to-noise ratio per pixel in the continuum at  $5100(1+z)$  Å.<sup>b</sup> The median air mass at which the spectra were obtained throughout the campaign.

the host-galaxy surface brightness was subtracted from each of the AGN images to help compensate for the diluting contribution from host-galaxy starlight. The models did not include a bulge component due to the lack of spatial resolution in the ground-based images, and so represent a lower limit to the true host-galaxy contribution. As we are interested here in relative flux changes, the absolute scaling of the AGN flux in the photometry is not important for the results described in this work.

Flux uncertainties were determined through two methods and the larger uncertainty contribution was adopted for each datum. In general, the flux errors from photon statistics were not large enough to account for the overall behavior of the light curves, and instead the uncertainty determined from the average difference between closely spaced pairs of points in each light curve was adopted. The exceptions were generally nights with poor weather conditions, where the photon-counting statistics provided a larger flux uncertainty. The *B*- and *V*-band light curves for each of the 13 AGNs are tabulated in Paper II.

## 2.2. Spectroscopy

Our spectroscopic campaign was carried out over 64 mostly contiguous nights at the Lick Observatory 3-m Shane telescope between 2008 March 25 and June 1. We used the Kast dual spectrograph but restricted our observations to the red-side CCD<sup>18</sup> and employed the 600 lines  $\text{mm}^{-1}$  grating with spectral coverage over the range 4300–7100 Å, giving a nominal resolution of  $2.35 \text{ Å pix}^{-1}$  in the dispersion direction and  $0''.78 \text{ pix}^{-1}$  in the spatial direction. Spectra were obtained through a  $4''$ -wide slit at fixed position angles for each of the objects (as listed in Table 2). A fixed position angle for each individual object is important to mitigate any apparent variability due to different contributions of starlight from structures within the host galaxy. The position angles were set to match the average parallactic angle expected for each of the objects throughout the length of the spectroscopic campaign, in an attempt to lessen the effect of atmospheric dispersion (Filippenko 1982). The number of

**Table 3**  
[O III]  $\lambda 5007$  Absolute Flux

Object	$f(\text{[O III]})$ ( $10^{-13} \text{ erg s}^{-1} \text{ cm}^{-2}$ )	$f(\text{[O III]})_{\text{lit}}$ ( $10^{-13} \text{ erg s}^{-1} \text{ cm}^{-2}$ )	Ref.
Mrk 142	0.321	0.20	1
SBS 1116+583A	0.158		
Arp 151	0.489	0.73	1
Mrk 1310	1.10		
Mrk 202	0.271		
NGC 4253	5.52	4.54	2
NGC 4748	3.50	3.65	2
IC 4218	0.181		
MCG -06-30-15	0.856	0.753, 1.14	2, 3
NGC 5548	5.55	5.49, 3.6, $5.58 \pm 0.27$	1, 2, 4
Mrk 290	2.75	2.40, 3.42	1, 5
IC 1198	0.751	0.61, 0.70	2, 3
NGC 6814	1.62	1.37, 1.44, 1.61	1, 3, 6

**References.** (1) Yee 1980; (2) de Grijp et al. 1992; (3) Morris & Ward 1988; (4) Peterson et al. 1991; (5) Weedman 1972; (6) Sekiguchi & Menzies 1990.

nights on which spectra were obtained for each of the objects in our sample ranged from 43 to 51, with an average of 47, which is fairly typical given the historic data on spring observing conditions at Lick Observatory.<sup>19</sup>

Exposure times, average air mass, and typical signal-to-noise ratio (S/N) per pixel in the continuum are also listed in Table 2. The two-dimensional spectroscopic images were reduced with IRAF<sup>20</sup> and an extraction width of 13 pixels (9 pixels for MCG -06-30-15, to avoid a nearby star) was applied, resulting in spectra with a  $10''.1$  ( $7''.0$ ) extraction. Sky regions were included on either side of the extracted regions, of width 6 pixels and beginning at a distance of 19 pixels to avoid the vast majority of contribution from the extended host galaxies. Flux calibrations were determined from nightly spectra of standard stars, which typically included Feige 34 and BD+284211.

To mitigate the effects of slit losses and variable seeing and transparency, a final, internal calibration of the spectra is required. We employed the spectral scaling algorithm of van Groningen & Wanders (1992) to scale the total flux of the narrow [O III]  $\lambda\lambda 4959, 5007$  doublet in each spectrum to match the [O III] flux in a reference spectrum created from the mean of the spectra obtained for each object. This method accounts for differences in the overall flux scale, as well as small wavelength shifts and small differences in spectral resolution due to variable seeing, and has been shown to result in spectrophotometric accuracies of  $\sim 2\%$  (Peterson et al. 1998a). The adopted absolute scaling of the [O III]  $\lambda 5007$  line for each object is listed in Table 3, along with spectrophotometric [O III]  $\lambda 5007$  fluxes from the literature for comparison. From the available information, it was determined that the night of 2008 April 10 was the only steadily photometric night of the campaign, and provides the absolute [O III] scaling for all the objects in our sample, with other clear nights suffering from haze, moderate to strong winds, or highly variable seeing.

The spectroscopic light curves were measured from the final, calibrated spectra for each object by fitting a local, linear continuum under the H $\beta$ + [O III] emission complex and integrat-

<sup>18</sup> Shortly before our spectroscopic campaign began, the blue-side CCD in the Kast spectrograph failed and was replaced by a temporary CCD with a much lower quantum efficiency. Rather than extending our exposure times and decreasing the sample of target AGNs, we opted to use only the red-side CCD.

<sup>19</sup> See [http://mthamilton.ucolick.org/techdocs/MH\\_weather/obstats/](http://mthamilton.ucolick.org/techdocs/MH_weather/obstats/) for average historic weather records for Lick Observatory.

<sup>20</sup> IRAF is distributed by the National Optical Astronomy Observatories, which are operated by the Association of Universities for Research in Astronomy, Inc., under cooperative agreement with the National Science Foundation.

**Table 4**  
H $\beta$  Continuum Windows and Integration Limits

Object	Continuum Windows		Line Limits	$\langle f(H\beta) \rangle$	$\langle f_{\lambda}(5100 \times (1+z)) \rangle$
	(Å)	(Å)	(Å)	( $10^{-13}$ erg s $^{-1}$ cm $^{-2}$ )	( $10^{-15}$ erg s $^{-1}$ cm $^{-2}$ Å $^{-1}$ )
Mrk 142	4960–5000	5300–5350	5045–5125	$0.928 \pm 0.080$	$2.05 \pm 0.19$
SBS 1116+583A	4875–4925	5200–5250	4925–5055	$0.262 \pm 0.028$	$1.088 \pm 0.067$
Arp 151	4850–4890	5175–5250	4900–5040	$0.86 \pm 0.15$	$1.21 \pm 0.15$
Mrk 1310	4850–4900	5150–5200	4900–5010	$0.495 \pm 0.054$	$1.87 \pm 0.12$
Mrk 202	4875–4925	5150–5200	4925–5025	$0.299 \pm 0.027$	$1.698 \pm 0.070$
NGC 4253	4820–4860	5150–5200	4860–4975	$1.99 \pm 0.10$	$4.59 \pm 0.26$
NGC 4748	4600–4650	5150–5200	4850–5000	$2.11 \pm 0.11$	$4.36 \pm 0.21$
IC 4218	4800–4850	5150–5200	4850–5030	$0.217 \pm 0.037$	$1.72 \pm 0.18$
MCG –06-30-15	4750–4800	5150–5200	4850–4940	$0.806 \pm 0.069$	$4.33 \pm 0.59$
NGC 5548	4725–4775	5150–5200	4775–5150	$3.39 \pm 0.33$	$6.12 \pm 0.38$
Mrk 290	4850–4900	5200–5250	4900–5085	$3.254 \pm 0.099$	$3.56 \pm 0.13$
IC 1198	4900–4940	5250–5300	4940–5100	$1.135 \pm 0.045$	$2.81 \pm 0.17$
NGC 6814	4540–4590	5100–5150	4800–4970	$2.81 \pm 0.26$	$6.47 \pm 0.50$

**Note.** The H $\beta$  fluxes above include the contribution from the narrow-line component; and the flux density at rest frame 5100 Å includes the contribution from host-galaxy starlight.

ing the H $\beta$  emission-line flux above the fitted continuum. This technique includes the flux contribution from the narrow H $\beta$  emission line, which is simply a constant offset in the resultant light curves. In the case of NGC 5548, the red wing of H $\beta$  extends underneath the [O III] emission lines, so the [O III] lines were removed prior to measuring the H $\beta$  flux. For NGC 6814, the continuum window to the blue of H $\beta$  had to be placed to the blue of the He II  $\lambda$ 4686 line as well to avoid contamination from that emission line. Table 4 gives the continuum windows and line integration limits for each object as well as the mean and standard deviation of the H $\beta$  flux. We also list the mean of the continua of the individual spectra as the flux density at  $5100 \times (1+z)$  Å. The H $\beta$  light curves for each of the objects are tabulated in Tables 5–7 and presented in Figures 1–4 along with the *B*- and *V*-band light curves.

Statistical properties of the H $\beta$  light curves are listed in Table 8 along with the properties of the *B*- and *V*-band light curves and the 5100 Å flux for comparison. Column (1) lists the object, Column (2) gives the measured feature, and Column (3) lists the number of measurements in each light curve. For our analysis, we binned all photometric measurements within 0.1 days. Columns (4) and (5) are the sampling intervals between data points, measured as the mean and the median, respectively. Column (6) gives the mean fractional error, which is based on the comparison of observations that are closely spaced in time. Occasionally, spectra were obtained under poor weather conditions and, in those cases, the uncertainties on the H $\beta$  fluxes are given by photon counting statistics instead. The “excess variance” in Column (7) is computed as

$$F_{\text{var}} = \frac{\sqrt{\sigma^2 - \delta^2}}{\langle f \rangle}, \quad (1)$$

where  $\sigma^2$  is the variance of the fluxes,  $\delta^2$  is their mean-square uncertainty, and  $\langle f \rangle$  is the mean of the observed fluxes. Finally, Column (8) is the ratio of the maximum to the minimum flux ( $R_{\text{max}}$ ) for each light curve.

### 3. ANALYSIS

#### 3.1. Time-series Analysis

For the time-series analysis, we consider both the *B*- and *V*-band photometric light curves as the driving, continuum light

curve. In general, they have similar sampling over the length of observations. The variability in the *B* band tends to be somewhat more pronounced than in the *V* band, most likely due to a smaller component of host-galaxy starlight dilution, and is easily seen by comparing the values of  $F_{\text{var}}$  and  $R_{\text{max}}$  for the *B*- and *V*-band observations of each object as listed in Table 8. As shown in Paper II, we find no evidence for a time lag between the variations in the *B* and *V* bands.

To determine the average time lag between variations in the continuum and variations in the H $\beta$  emission-line flux, we follow the standard practice of cross-correlating the light curves. Specifically, we employ the interpolation cross-correlation function (CCF) method (Gaskell & Sparke 1986; Gaskell & Peterson 1987) with the modifications described by White & Peterson (1994). The method measures the CCF between two light curves twice: first by interpolating between the continuum points, and second by interpolating between the emission-line points. The average of the two results is the final CCF. Following Peterson et al. (2004), each CCF is characterized by the maximum cross-correlation coefficient ( $r_{\text{max}}$ ), the time delay corresponding to the location of  $r_{\text{max}}$  ( $\tau_{\text{peak}}$ ), and the centroid of the points about the peak ( $\tau_{\text{cent}}$ ) above some threshold value, typically  $0.8r_{\text{max}}$ .

Figures 1–4 show the CCFs for the 13 AGNs in our sample. As mentioned above, we cross-correlated the H $\beta$  flux with both the *B*- and *V*-band light curves, and we show the results of both for comparison. We also show the auto-correlation functions for the photometric light curves, which, as expected, peak at a time lag of zero days. Four of the objects do not appear to show a significant lag signal in their CCFs. IC 4218 has a broad, flat-topped (H $\beta$  versus *B*) or double-horned (H $\beta$  versus *V*) CCF structure centered around zero lag. MCG –06-30-15 shows a noisy CCF profile that appears to be consistent with zero at all lag times. Mrk 290 has a very slowly rising and flat-topped CCF profile at positive lag times. Inspection of the H $\beta$  variations in this object does not seem to show an echo of the photometric variations, and there is no H $\beta$  signal in the variable spectrum of Mrk 290. And IC 1198 shows a CCF profile that is rather noisy and centered about zero at all lag times, with the largest peak occurring at a lag of  $\sim -22$  days. There does not appear to be any signal from H $\beta$  in the variable spectrum of this object either.

While it is quite simple to determine the lag time between two time series by measuring either  $\tau_{\text{peak}}$  or  $\tau_{\text{cent}}$ , it is more



**Table 5**  
H $\beta$  Light Curves—Mrk 142, SBS 1116+583A, Arp 151, Mrk 1310, and Mrk 202

Mrk 142		SBS 1116+583A		Arp 151		Mrk 1310		Mrk 202	
HJD	$f(\text{H}\beta)$	HJD	$f(\text{H}\beta)$	HJD	$f(\text{H}\beta)$	HJD	$f(\text{H}\beta)$	HJD	$f(\text{H}\beta)$
4550.6599	0.943 $\pm$ 0.011	4550.6925	0.3150 $\pm$ 0.0088	4550.7180	0.791 $\pm$ 0.012	4550.7726	0.4448 $\pm$ 0.0081	4550.7434	0.2805 $\pm$ 0.0035
4551.6560	0.859 $\pm$ 0.010	4551.7189	0.3013 $\pm$ 0.0084	4551.7478	0.770 $\pm$ 0.012	4551.8100	0.4793 $\pm$ 0.0088	4551.7693	0.2822 $\pm$ 0.0035
4553.6576	0.945 $\pm$ 0.011	4553.7176	0.3009 $\pm$ 0.0084	4553.7470	0.733 $\pm$ 0.011	4553.8092	0.5196 $\pm$ 0.0095	4553.7721	0.2995 $\pm$ 0.0037
4555.8322	1.255 $\pm$ 0.014	4555.8587	0.2767 $\pm$ 0.0077	4556.7118	0.647 $\pm$ 0.010	4556.7724	0.5427 $\pm$ 0.0099	4556.7381	0.2711 $\pm$ 0.0034
4556.6591	0.947 $\pm$ 0.011	4556.6866	0.2743 $\pm$ 0.0077	4557.7555	0.644 $\pm$ 0.010	4557.8255	0.5583 $\pm$ 0.0102	4557.7884	0.2677 $\pm$ 0.0034
4557.6574	0.925 $\pm$ 0.010	4557.6847	0.2615 $\pm$ 0.0073	4558.6902	0.632 $\pm$ 0.009	4558.7907	0.5608 $\pm$ 0.0103	4558.7121	0.2506 $\pm$ 0.0031
4558.6464	0.981 $\pm$ 0.011	4558.6633	0.2710 $\pm$ 0.0076	4559.8700	0.619 $\pm$ 0.009	4559.9485	0.5503 $\pm$ 0.0101	4559.9658	0.2556 $\pm$ 0.0032
4559.8879	0.899 $\pm$ 0.010	4559.9038	0.2607 $\pm$ 0.0073	4560.6570	0.638 $\pm$ 0.010	4560.7912	0.5377 $\pm$ 0.0098	4560.7389	0.2587 $\pm$ 0.0032
4560.6809	0.960 $\pm$ 0.011	4560.7082	0.2556 $\pm$ 0.0071	4561.6791	0.637 $\pm$ 0.010	4561.8143	0.4968 $\pm$ 0.0091	4561.7450	0.2516 $\pm$ 0.0031
4561.7065	0.875 $\pm$ 0.010	4561.7268	0.2358 $\pm$ 0.0066	4562.7017	0.622 $\pm$ 0.009	4562.7961	0.4686 $\pm$ 0.0086	4562.7600	0.2522 $\pm$ 0.0032
4562.7222	0.972 $\pm$ 0.011	4562.7373	0.2419 $\pm$ 0.0068	4564.7136	0.673 $\pm$ 0.010	4564.7669	0.4225 $\pm$ 0.0077	4564.7344	0.2731 $\pm$ 0.0034
4564.6609	0.937 $\pm$ 0.011	4564.6890	0.2674 $\pm$ 0.0075	4566.7181	0.692 $\pm$ 0.010	4566.7677	0.3993 $\pm$ 0.0073	4566.7384	0.2922 $\pm$ 0.0037
4566.6662	0.952 $\pm$ 0.011	4566.6937	0.2307 $\pm$ 0.0064	4567.7170	0.743 $\pm$ 0.011	4567.7764	0.4129 $\pm$ 0.0076	4567.7396	0.2855 $\pm$ 0.0036
4567.6650	0.968 $\pm$ 0.011	4567.6924	0.2293 $\pm$ 0.0064	4568.7177	0.759 $\pm$ 0.011	4568.7689	0.4213 $\pm$ 0.0077	4568.7380	0.2891 $\pm$ 0.0036
4568.6636	0.963 $\pm$ 0.011	4568.6919	0.2187 $\pm$ 0.0061	4569.7258	0.760 $\pm$ 0.011	4569.7798	0.4200 $\pm$ 0.0077	4569.7496	0.2899 $\pm$ 0.0036
4569.6805	0.979 $\pm$ 0.011	4569.7050	0.2280 $\pm$ 0.0064	4570.7526	0.786 $\pm$ 0.012	4570.8030	0.4363 $\pm$ 0.0080	4570.7727	0.2965 $\pm$ 0.0037
4570.6594	0.961 $\pm$ 0.011	4570.7310	0.2312 $\pm$ 0.0065	4572.7551	0.864 $\pm$ 0.013	4575.7581	0.4908 $\pm$ 0.0162	4572.8944	0.2922 $\pm$ 0.0037
4572.6842	0.921 $\pm$ 0.010	4572.7106	0.2439 $\pm$ 0.0068	4573.7215	0.919 $\pm$ 0.014	4581.7875	0.5216 $\pm$ 0.0096	4573.7419	0.2945 $\pm$ 0.0037
4573.6698	0.937 $\pm$ 0.011	4573.6979	0.2705 $\pm$ 0.0076	4575.6875	0.954 $\pm$ 0.014	4582.7344	0.4841 $\pm$ 0.0089	4575.8692	0.2691 $\pm$ 0.0034
4575.7090	0.637 $\pm$ 0.007	4575.9200	0.2935 $\pm$ 0.0082	4581.7317	0.974 $\pm$ 0.015	4583.7331	0.4987 $\pm$ 0.0091	4581.7533	0.3076 $\pm$ 0.0039
4581.6673	0.929 $\pm$ 0.010	4581.7033	0.2796 $\pm$ 0.0078	4582.8300	1.010 $\pm$ 0.015	4584.7524	0.4851 $\pm$ 0.0089	4582.7752	0.3249 $\pm$ 0.0041
4582.6672	0.900 $\pm$ 0.010	4582.6997	0.2714 $\pm$ 0.0076	4583.8341	0.987 $\pm$ 0.015	4585.7278	0.4607 $\pm$ 0.0084	4583.7754	0.3218 $\pm$ 0.0040
4583.6648	0.905 $\pm$ 0.010	4583.6927	0.2750 $\pm$ 0.0077	4584.7895	0.977 $\pm$ 0.015	4587.7413	0.4731 $\pm$ 0.0087	4584.8230	0.2843 $\pm$ 0.0036
4584.6796	0.846 $\pm$ 0.010	4584.7176	0.2226 $\pm$ 0.0062	4585.8605	1.014 $\pm$ 0.015	4588.7303	0.5137 $\pm$ 0.0094	4585.9011	0.3079 $\pm$ 0.0039
4585.6626	0.821 $\pm$ 0.009	4585.6924	0.2288 $\pm$ 0.0064	4587.7764	1.049 $\pm$ 0.016	4589.7353	0.4965 $\pm$ 0.0091	4587.9043	0.2983 $\pm$ 0.0037
4587.6776	0.931 $\pm$ 0.010	4587.7063	0.2426 $\pm$ 0.0068	4588.7821	1.074 $\pm$ 0.016	4590.7365	0.4496 $\pm$ 0.0082	4588.8947	0.3137 $\pm$ 0.0039
4588.6690	0.910 $\pm$ 0.010	4588.6966	0.2431 $\pm$ 0.0068	4589.7693	1.060 $\pm$ 0.016	4591.7273	0.4599 $\pm$ 0.0084	4589.9091	0.2915 $\pm$ 0.0036
4589.6708	0.861 $\pm$ 0.010	4589.7006	0.2445 $\pm$ 0.0068	4590.7677	1.046 $\pm$ 0.016	4592.7303	0.4641 $\pm$ 0.0085	4590.9006	0.3121 $\pm$ 0.0039
4590.6762	0.900 $\pm$ 0.010	4590.7037	0.2401 $\pm$ 0.0067	4591.7584	1.060 $\pm$ 0.016	4593.7325	0.4493 $\pm$ 0.0082	4591.9069	0.2942 $\pm$ 0.0037
4591.6675	0.890 $\pm$ 0.010	4591.6948	0.2645 $\pm$ 0.0074	4592.7618	1.027 $\pm$ 0.015	4594.7361	0.4602 $\pm$ 0.0084	4592.9010	0.3124 $\pm$ 0.0039
4592.6697	0.942 $\pm$ 0.011	4592.6977	0.2773 $\pm$ 0.0077	4593.7636	0.913 $\pm$ 0.014	4595.7465	0.4639 $\pm$ 0.0085	4593.9007	0.2960 $\pm$ 0.0037
4593.6707	0.918 $\pm$ 0.010	4593.6993	0.2831 $\pm$ 0.0079	4594.8047	1.003 $\pm$ 0.015	4596.7329	0.5186 $\pm$ 0.0095	4594.8703	0.2987 $\pm$ 0.0037
4594.6761	0.910 $\pm$ 0.010	4594.7031	0.2809 $\pm$ 0.0078	4595.8015	0.948 $\pm$ 0.014	4597.7353	0.5064 $\pm$ 0.0093	4595.8579	0.2964 $\pm$ 0.0037
4595.6869	0.855 $\pm$ 0.010	4595.7145	0.2823 $\pm$ 0.0079	4596.8003	0.978 $\pm$ 0.015	4598.7316	0.5358 $\pm$ 0.0098	4596.8908	0.2938 $\pm$ 0.0037
4597.1746	0.995 $\pm$ 0.011	4596.7005	0.3058 $\pm$ 0.0085	4597.8005	0.945 $\pm$ 0.014	4600.7030	0.5400 $\pm$ 0.0099	4597.8964	0.2997 $\pm$ 0.0038
4597.6761	0.904 $\pm$ 0.010	4597.7035	0.2888 $\pm$ 0.0081	4598.8010	0.846 $\pm$ 0.021	4602.7830	0.6463 $\pm$ 0.0118	4601.8116	0.3216 $\pm$ 0.0040
4598.6721	0.896 $\pm$ 0.010	4598.6992	0.3034 $\pm$ 0.0085	4600.7205	0.954 $\pm$ 0.014	4603.7310	0.6206 $\pm$ 0.0114	4602.9024	0.3408 $\pm$ 0.0043
4600.6732	0.917 $\pm$ 0.010	4600.8294	0.2653 $\pm$ 0.0074	4601.7713	0.928 $\pm$ 0.014	4604.7232	0.5865 $\pm$ 0.0107	4603.8855	0.3343 $\pm$ 0.0042
4601.6753	0.922 $\pm$ 0.010	4601.7108	0.2936 $\pm$ 0.0082	4602.8002	0.912 $\pm$ 0.014	4605.7092	0.5888 $\pm$ 0.0108	4604.9140	0.3554 $\pm$ 0.0044
4602.8195	0.905 $\pm$ 0.010	4602.8731	0.2864 $\pm$ 0.0080	4603.8428	0.873 $\pm$ 0.013	4607.7142	0.5411 $\pm$ 0.0099	4605.8939	0.3407 $\pm$ 0.0043
4603.6917	0.896 $\pm$ 0.010	4604.8290	0.2642 $\pm$ 0.0074	4604.8036	0.837 $\pm$ 0.013	4608.7901	0.4663 $\pm$ 0.0085	4612.8862	0.3151 $\pm$ 0.0039
4604.6891	0.914 $\pm$ 0.010	4605.8064	0.2957 $\pm$ 0.0083	4605.7268	0.846 $\pm$ 0.013	4612.7931	0.4576 $\pm$ 0.0084	4613.8602	0.3185 $\pm$ 0.0040
4605.6784	0.905 $\pm$ 0.010	4607.8182	0.2171 $\pm$ 0.0061	4607.7301	0.791 $\pm$ 0.012	4613.7813	0.5243 $\pm$ 0.0096	4614.8871	0.3116 $\pm$ 0.0039
4607.6841	0.913 $\pm$ 0.010	4608.8160	0.2170 $\pm$ 0.0061			4615.7819	0.4884 $\pm$ 0.0089	4615.8847	0.3514 $\pm$ 0.0044
4608.6829	0.950 $\pm$ 0.011	4612.8142	0.2396 $\pm$ 0.0067			4616.7337	0.4694 $\pm$ 0.0086	4616.8548	0.3364 $\pm$ 0.0042
4613.6800	0.949 $\pm$ 0.011	4613.8024	0.2611 $\pm$ 0.0073			4617.7604	0.4647 $\pm$ 0.0085	4617.8826	0.3433 $\pm$ 0.0043
4614.6846	0.856 $\pm$ 0.010	4615.8328	0.2356 $\pm$ 0.0066			4618.7642	0.4511 $\pm$ 0.0083		
4615.6835	1.072 $\pm$ 0.012	4616.7816	0.2132 $\pm$ 0.0060						
4616.7547	0.992 $\pm$ 0.011	4617.8077	0.2587 $\pm$ 0.0072						
4617.6966	0.899 $\pm$ 0.010	4618.7821	0.3079 $\pm$ 0.0086						
4618.6954	1.114 $\pm$ 0.013								

**Note.** HJD = Heliocentric Julian Day  $-2,450,000$ ; H $\beta$  emission-line fluxes are in units of  $10^{-13}$  erg s $^{-1}$  cm $^{-2}$ .

difficult to quantify the uncertainty in the measured lag time. The standard procedure is to employ the Monte Carlo “flux randomization/random subset sampling” method described by Peterson et al. (1998b, 2004). The method takes  $N$  random and independent samplings from the  $N$  points available in the light curves, regardless of whether a datum has been already sampled. The uncertainty for a point that is sampled  $1 \leq n \leq N$  times is scaled by a factor of  $n^{1/2}$ , and in general

the fraction of points that are not selected in any particular realization is  $\sim 1/e$ . This “random subset sampling” helps to quantify the uncertainty in the lag time that arises based on the contribution from individual points in the light curve. The flux values in this randomly sampled subset are then randomly altered by a Gaussian deviation of the flux uncertainty. This “flux randomization” accounts for the uncertainty in the measured flux values. The CCF is calculated for the sampled

**Table 6**  
H $\beta$  Light Curves—NGC 4253, NGC 4748, IC 4218, MCG –06-30-15, and NGC 5548

NGC 4253		NGC 4748		IC 4218		MCG –06-30-15		NGC 5548	
HJD	$f(\text{H}\beta)$	HJD	$f(\text{H}\beta)$	HJD	$f(\text{H}\beta)$	HJD	$f(\text{H}\beta)$	HJD	$f(\text{H}\beta)$
4550.8014	1.985 $\pm$ 0.017	4550.8173	1.987 $\pm$ 0.017	4550.9372	0.263 $\pm$ 0.014	4550.9007	0.773 $\pm$ 0.031	4550.8678	3.341 $\pm$ 0.052
4551.8338	1.948 $\pm$ 0.017	4551.8530	1.978 $\pm$ 0.017	4551.9372	0.234 $\pm$ 0.013	4551.8929	0.771 $\pm$ 0.031	4551.8664	3.386 $\pm$ 0.052
4553.8298	2.031 $\pm$ 0.017	4553.8454	1.983 $\pm$ 0.017	4556.8372	0.267 $\pm$ 0.014	4553.8838	0.772 $\pm$ 0.031	4553.8626	3.372 $\pm$ 0.052
4555.9872	1.858 $\pm$ 0.031	4556.8087	1.887 $\pm$ 0.017	4558.8351	0.271 $\pm$ 0.015	4556.8813	0.780 $\pm$ 0.032	4556.8589	3.308 $\pm$ 0.051
4556.7926	1.997 $\pm$ 0.017	4557.8618	1.913 $\pm$ 0.017	4560.8290	0.260 $\pm$ 0.014	4557.9053	0.866 $\pm$ 0.035	4557.8755	3.344 $\pm$ 0.052
4557.7073	2.097 $\pm$ 0.018	4558.8076	1.953 $\pm$ 0.017	4561.8328	0.232 $\pm$ 0.013	4558.8788	0.830 $\pm$ 0.034	4558.8595	3.181 $\pm$ 0.049
4558.6802	2.094 $\pm$ 0.018	4560.8578	1.965 $\pm$ 0.017	4562.8158	0.237 $\pm$ 0.013	4560.8720	0.888 $\pm$ 0.036	4559.9903	3.282 $\pm$ 0.051
4559.9827	2.138 $\pm$ 0.018	4561.8522	1.930 $\pm$ 0.017	4566.8828	0.211 $\pm$ 0.011	4561.8670	0.683 $\pm$ 0.028	4560.8967	3.277 $\pm$ 0.051
4560.7659	2.109 $\pm$ 0.018	4562.8377	1.894 $\pm$ 0.017	4567.8865	0.204 $\pm$ 0.011	4562.8549	0.696 $\pm$ 0.028	4562.9997	3.398 $\pm$ 0.053
4561.7998	2.040 $\pm$ 0.018	4564.8024	2.046 $\pm$ 0.018	4568.8743	0.228 $\pm$ 0.012	4566.8546	0.799 $\pm$ 0.032	4564.9405	3.761 $\pm$ 0.557
4562.7806	2.113 $\pm$ 0.018	4566.8071	2.012 $\pm$ 0.018	4569.9003	0.239 $\pm$ 0.013	4567.8529	0.808 $\pm$ 0.033	4566.9017	3.509 $\pm$ 0.054
4564.7862	2.124 $\pm$ 0.018	4567.8104	2.010 $\pm$ 0.018	4570.8983	0.219 $\pm$ 0.012	4568.8453	0.836 $\pm$ 0.034	4567.8218	3.495 $\pm$ 0.054
4566.7916	2.070 $\pm$ 0.018	4568.8070	2.058 $\pm$ 0.018	4573.7922	0.251 $\pm$ 0.014	4569.8506	0.870 $\pm$ 0.035	4568.8201	3.594 $\pm$ 0.056
4567.7949	2.081 $\pm$ 0.018	4569.7977	2.083 $\pm$ 0.018	4581.8880	0.188 $\pm$ 0.010	4570.8414	0.822 $\pm$ 0.033	4569.8830	3.628 $\pm$ 0.056
4568.7896	2.082 $\pm$ 0.018	4570.8224	2.020 $\pm$ 0.018	4582.8930	0.234 $\pm$ 0.013	4572.8345	0.852 $\pm$ 0.034	4570.8760	3.605 $\pm$ 0.056
4569.8729	2.050 $\pm$ 0.018	4572.8723	2.100 $\pm$ 0.018	4583.8888	0.209 $\pm$ 0.011	4573.8404	0.872 $\pm$ 0.035	4572.9341	3.539 $\pm$ 0.055
4570.8633	2.054 $\pm$ 0.018	4573.7696	2.122 $\pm$ 0.019	4584.8577	0.183 $\pm$ 0.010	4575.8398	0.729 $\pm$ 0.029	4573.8140	3.548 $\pm$ 0.055
4572.9156	2.019 $\pm$ 0.018	4581.8356	2.187 $\pm$ 0.019	4585.7753	0.163 $\pm$ 0.009	4581.8155	0.775 $\pm$ 0.031	4575.9500	3.386 $\pm$ 0.081
4573.8639	2.058 $\pm$ 0.018	4582.7554	2.150 $\pm$ 0.019	4587.8627	0.189 $\pm$ 0.010	4582.8097	0.832 $\pm$ 0.034	4581.9237	3.479 $\pm$ 0.054
4575.8961	2.049 $\pm$ 0.018	4583.7544	2.160 $\pm$ 0.019	4588.8565	0.200 $\pm$ 0.011	4583.8102	0.834 $\pm$ 0.034	4582.9322	3.567 $\pm$ 0.055
4581.9089	2.000 $\pm$ 0.017	4584.7718	2.146 $\pm$ 0.019	4589.8671	0.205 $\pm$ 0.011	4587.8043	0.789 $\pm$ 0.032	4583.9276	3.511 $\pm$ 0.054
4582.9155	2.036 $\pm$ 0.017	4585.7473	2.115 $\pm$ 0.019	4590.8627	0.194 $\pm$ 0.010	4589.8018	0.761 $\pm$ 0.031	4584.8941	3.649 $\pm$ 0.057
4583.9107	2.008 $\pm$ 0.017	4587.7612	2.173 $\pm$ 0.019	4591.8663	0.186 $\pm$ 0.010	4590.8007	0.837 $\pm$ 0.034	4585.9384	3.746 $\pm$ 0.058
4584.8792	2.028 $\pm$ 0.017	4588.7502	2.238 $\pm$ 0.020	4592.8623	0.195 $\pm$ 0.011	4591.7959	0.786 $\pm$ 0.032	4587.9254	3.903 $\pm$ 0.060
4585.8815	2.032 $\pm$ 0.017	4589.7575	2.271 $\pm$ 0.020	4593.8630	0.165 $\pm$ 0.009	4592.7947	0.772 $\pm$ 0.031	4588.9167	3.882 $\pm$ 0.060
4587.8867	1.949 $\pm$ 0.017	4590.7558	2.182 $\pm$ 0.019	4594.8339	0.177 $\pm$ 0.010	4593.7952	0.791 $\pm$ 0.032	4589.9298	3.844 $\pm$ 0.060
4588.8780	2.048 $\pm$ 0.018	4591.7470	2.214 $\pm$ 0.019	4595.8284	0.170 $\pm$ 0.009	4594.7825	0.727 $\pm$ 0.030	4590.9214	3.872 $\pm$ 0.060
4589.8875	2.001 $\pm$ 0.017	4592.7507	2.164 $\pm$ 0.019	4596.8309	0.183 $\pm$ 0.010	4595.7851	0.737 $\pm$ 0.030	4591.9278	3.766 $\pm$ 0.058
4590.8825	2.025 $\pm$ 0.017	4593.7517	2.160 $\pm$ 0.019	4597.8582	0.167 $\pm$ 0.009	4596.7772	0.815 $\pm$ 0.033	4592.9217	3.764 $\pm$ 0.058
4591.8896	1.980 $\pm$ 0.017	4594.7569	2.231 $\pm$ 0.020	4601.8491	0.224 $\pm$ 0.013	4597.7787	0.832 $\pm$ 0.034	4593.9218	3.807 $\pm$ 0.059
4592.8844	1.977 $\pm$ 0.017	4595.7658	2.253 $\pm$ 0.020	4604.8890	0.173 $\pm$ 0.009	4598.7755	0.735 $\pm$ 0.030	4594.9230	3.599 $\pm$ 0.056
4593.8831	1.928 $\pm$ 0.017	4596.7525	2.281 $\pm$ 0.020	4605.8573	0.165 $\pm$ 0.090	4600.7774	0.834 $\pm$ 0.034	4595.9071	3.710 $\pm$ 0.057
4594.8536	1.890 $\pm$ 0.016	4597.7547	2.237 $\pm$ 0.020	4607.8548	0.267 $\pm$ 0.015	4601.7573	0.838 $\pm$ 0.034	4596.9126	3.626 $\pm$ 0.056
4595.8405	1.975 $\pm$ 0.017	4598.7508	2.264 $\pm$ 0.020	4608.8580	0.193 $\pm$ 0.016	4602.7605	0.890 $\pm$ 0.036	4597.9181	3.535 $\pm$ 0.055
4596.8745	1.887 $\pm$ 0.016	4600.7957	2.258 $\pm$ 0.020	4611.8449	0.231 $\pm$ 0.013	4603.7690	0.689 $\pm$ 0.028	4598.8420	3.475 $\pm$ 0.090
4597.8779	1.932 $\pm$ 0.017	4601.7432	2.134 $\pm$ 0.019	4612.8694	0.230 $\pm$ 0.012	4604.7505	0.792 $\pm$ 0.032	4600.8564	3.301 $\pm$ 0.051
4598.8237	1.602 $\pm$ 0.148	4602.7264	2.103 $\pm$ 0.118	4613.8330	0.294 $\pm$ 0.116	4605.7525	0.824 $\pm$ 0.133	4601.8688	3.234 $\pm$ 0.050
4600.7503	1.906 $\pm$ 0.016	4603.8304	2.305 $\pm$ 0.020	4615.8112	0.279 $\pm$ 0.015	4607.7576	1.097 $\pm$ 0.101	4602.9239	3.274 $\pm$ 0.051
4601.7961	1.931 $\pm$ 0.017	4604.8659	2.172 $\pm$ 0.019	4616.8177	0.258 $\pm$ 0.014	4608.7375	0.763 $\pm$ 0.031	4603.9194	3.124 $\pm$ 0.053
4602.7378	1.954 $\pm$ 0.017	4605.8354	2.209 $\pm$ 0.019	4617.8407	0.259 $\pm$ 0.014	4613.7611	0.780 $\pm$ 0.061	4604.9353	3.225 $\pm$ 0.050
4603.8652	1.972 $\pm$ 0.017	4607.7997	2.073 $\pm$ 0.073			4614.7309	0.826 $\pm$ 0.033	4605.9149	3.064 $\pm$ 0.047
4605.8768	1.934 $\pm$ 0.017	4608.7163	2.085 $\pm$ 0.018			4615.7294	0.827 $\pm$ 0.033	4607.8999	3.131 $\pm$ 0.048
4607.8742	1.862 $\pm$ 0.016	4614.7131	2.097 $\pm$ 0.018					4608.9063	3.123 $\pm$ 0.050
4608.8813	1.701 $\pm$ 0.015	4615.7067	2.118 $\pm$ 0.019					4611.9246	2.968 $\pm$ 0.796
4613.8473	2.053 $\pm$ 0.018	4618.7451	2.075 $\pm$ 0.018					4612.9069	2.770 $\pm$ 0.043
4614.8695	1.988 $\pm$ 0.017							4613.9068	2.492 $\pm$ 0.553
4615.8665	1.966 $\pm$ 0.017							4614.9259	2.771 $\pm$ 0.043
4616.8365	1.935 $\pm$ 0.017							4615.9124	3.043 $\pm$ 0.047
4617.8594	1.921 $\pm$ 0.016							4616.9108	2.949 $\pm$ 0.046
4618.8351	2.157 $\pm$ 0.143							4617.9020	2.990 $\pm$ 0.046
								4618.8734	2.793 $\pm$ 0.091

**Note.** HJD = Heliocentric Julian Day –2,450,000; H $\beta$  emission-line fluxes are in units of  $10^{-13}$  erg s $^{-1}$  cm $^{-2}$ .

and modified light curves, and  $r_{\text{max}}$ ,  $\tau_{\text{cent}}$ , and  $\tau_{\text{peak}}$  are measured and recorded. The process is repeated for 1000 realizations, and distributions of correlation measurements are built up. The means of the cross-correlation centroid distribution and the cross-correlation peak distribution are taken to be  $\tau_{\text{cent}}$  and  $\tau_{\text{peak}}$ , respectively. The uncertainties on  $\tau_{\text{cent}}$  and  $\tau_{\text{peak}}$  are set such that 15.87% of the realizations fall above and 15.87% fall below the range of uncertainties, corresponding to  $\pm 1\sigma$  for a Gaussian distribution.

Table 9 lists the measured lag times and uncertainties for the nine objects with significant H $\beta$  lag signatures in their CCFs. Also listed are the lag times and uncertainties after correction for the time-dilation factor of  $1+z$ .

### 3.2. Line-width Measurement

Figure 5 shows the mean and root mean square (rms) spectra in the region around H $\beta$  for the nine objects with significant H $\beta$  lags. For comparison, we include in Figure 6 the mean

**Table 7**  
H $\beta$  Light Curves—Mrk 290, IC 1198, and NGC 6814

Mrk 290		IC 1198		NGC 6814	
HJD	$f(\text{H}\beta)$	HJD	$f(\text{H}\beta)$	HJD	$f(\text{H}\beta)$
4550.9734	$3.438 \pm 0.061$	4551.0023	$1.186 \pm 0.019$	4551.0180	$2.987 \pm 0.030$
4551.9662	$3.383 \pm 0.060$	4552.0039	$1.145 \pm 0.018$	4552.0264	$2.693 \pm 0.027$
4555.9998	$3.401 \pm 0.060$	4556.0233	$1.163 \pm 0.018$	4556.0339	$2.562 \pm 0.035$
4556.9015	$3.442 \pm 0.061$	4556.9309	$1.190 \pm 0.019$	4557.0200	$2.956 \pm 0.030$
4558.8995	$3.443 \pm 0.061$	4558.9231	$1.190 \pm 0.019$	4560.0402	$2.924 \pm 0.037$
4559.9990	$3.399 \pm 0.060$	4560.0230	$1.172 \pm 0.018$	4561.0266	$3.042 \pm 0.031$
4560.9107	$3.348 \pm 0.030$	4560.9417	$1.175 \pm 0.019$	4564.0146	$3.096 \pm 0.032$
4563.0117	$3.253 \pm 0.058$	4566.9602	$1.180 \pm 0.019$	4567.0021	$3.266 \pm 0.033$
4563.9912	$3.396 \pm 0.060$	4567.9748	$1.136 \pm 0.018$	4568.0082	$3.138 \pm 0.032$
4566.9350	$3.346 \pm 0.060$	4568.9233	$1.158 \pm 0.018$	4569.0070	$3.160 \pm 0.032$
4567.9476	$3.248 \pm 0.058$	4570.9537	$1.159 \pm 0.018$	4570.0003	$3.139 \pm 0.032$
4568.8957	$3.337 \pm 0.059$	4572.9665	$1.151 \pm 0.018$	4570.9899	$3.127 \pm 0.032$
4569.9151	$3.284 \pm 0.058$	4573.9507	$1.145 \pm 0.018$	4572.9883	$3.173 \pm 0.032$
4570.9189	$3.307 \pm 0.059$	4575.9921	$1.071 \pm 0.017$	4573.9952	$3.027 \pm 0.031$
4572.9434	$3.269 \pm 0.058$	4581.9628	$1.148 \pm 0.018$	4576.0113	$3.109 \pm 0.032$
4573.9102	$3.273 \pm 0.058$	4582.9746	$1.151 \pm 0.018$	4581.9978	$2.713 \pm 0.028$
4575.9693	$3.189 \pm 0.057$	4583.9707	$1.156 \pm 0.018$	4583.0102	$2.695 \pm 0.027$
4581.9349	$3.131 \pm 0.056$	4584.9733	$1.147 \pm 0.018$	4584.0028	$2.555 \pm 0.026$
4582.9459	$3.204 \pm 0.057$	4585.9815	$1.108 \pm 0.017$	4585.0027	$2.544 \pm 0.026$
4583.9414	$3.232 \pm 0.057$	4587.9626	$1.116 \pm 0.018$	4586.0112	$2.438 \pm 0.025$
4584.9398	$3.111 \pm 0.055$	4588.9532	$1.165 \pm 0.018$	4588.0005	$2.571 \pm 0.026$
4585.9516	$3.168 \pm 0.056$	4589.9672	$1.142 \pm 0.018$	4588.9927	$2.646 \pm 0.027$
4587.9360	$3.101 \pm 0.055$	4590.9588	$1.165 \pm 0.018$	4590.0043	$2.627 \pm 0.027$
4588.9259	$3.174 \pm 0.056$	4591.9632	$1.123 \pm 0.018$	4590.9920	$2.745 \pm 0.028$
4589.9395	$3.157 \pm 0.056$	4592.9575	$1.149 \pm 0.018$	4591.9933	$2.602 \pm 0.026$
4590.9318	$3.175 \pm 0.056$	4593.9851	$1.096 \pm 0.017$	4592.9872	$2.687 \pm 0.027$
4591.9369	$3.153 \pm 0.056$	4594.9590	$1.141 \pm 0.018$	4593.9387	$2.627 \pm 0.027$
4592.9306	$3.235 \pm 0.058$	4595.9419	$1.150 \pm 0.018$	4594.9950	$2.816 \pm 0.029$
4593.9584	$3.196 \pm 0.057$	4596.9490	$1.184 \pm 0.019$	4595.9770	$2.815 \pm 0.029$
4594.9322	$3.186 \pm 0.057$	4597.9552	$1.151 \pm 0.018$	4596.9783	$2.867 \pm 0.029$
4595.9160	$3.265 \pm 0.058$	4598.9350	$0.989 \pm 0.146$	4597.9865	$2.941 \pm 0.030$
4596.9218	$3.286 \pm 0.058$	4600.8938	$1.144 \pm 0.018$	4598.9686	$2.711 \pm 0.131$
4597.9287	$3.168 \pm 0.056$	4601.9382	$1.102 \pm 0.017$	4600.9250	$2.999 \pm 0.031$
4598.8656	$3.084 \pm 0.055$	4602.9611	$1.115 \pm 0.018$	4601.9789	$2.911 \pm 0.030$
4600.8656	$3.196 \pm 0.057$	4603.9591	$1.106 \pm 0.017$	4602.9915	$3.027 \pm 0.031$
4601.9111	$3.161 \pm 0.056$	4604.9686	$1.075 \pm 0.017$	4603.9917	$3.018 \pm 0.031$
4602.9344	$3.177 \pm 0.157$	4605.9503	$1.116 \pm 0.018$	4604.9922	$3.074 \pm 0.031$
4603.9305	$3.237 \pm 0.058$	4608.9364	$1.091 \pm 0.017$	4605.9838	$2.970 \pm 0.030$
4604.9449	$3.235 \pm 0.058$	4612.9481	$1.114 \pm 0.018$	4608.9747	$2.639 \pm 0.027$
4605.9238	$3.235 \pm 0.058$	4613.9446	$0.991 \pm 0.016$	4612.9746	$2.469 \pm 0.025$
4607.9123	$3.284 \pm 0.058$	4614.9681	$1.114 \pm 0.018$	4613.9797	$2.066 \pm 0.136$
4612.9202	$3.239 \pm 0.058$	4615.9499	$1.153 \pm 0.018$	4614.9871	$2.522 \pm 0.026$
4613.9228	$3.143 \pm 0.056$	4616.9462	$1.063 \pm 0.017$	4616.9777	$2.600 \pm 0.026$
4614.9427	$3.241 \pm 0.058$	4617.9372	$1.159 \pm 0.018$	4617.9693	$2.332 \pm 0.024$
4615.9226	$3.313 \pm 0.059$	4618.9607	$1.203 \pm 0.019$	4618.9885	$2.585 \pm 0.026$
4616.9199	$3.154 \pm 0.056$				
4617.9115	$3.407 \pm 0.061$				
4618.9014	$3.415 \pm 0.061$				

**Note.** HJD = Heliocentric Julian Day  $-2,450,000$ ; H $\beta$  emission-line fluxes are in units of  $10^{-13}$  erg s $^{-1}$  cm $^{-2}$ .

and rms spectra of the four objects with weak variability. The rms spectra show the standard deviation of all the individual spectra relative to the mean spectrum for an object, and are thus useful for visualizing and quantifying the variable components of the spectra. We also show the narrow-line subtracted mean and rms spectra in Figure 5 (except for Mrk 142 which appears to have Fe II emission blended with the [O III] emission in the mean spectrum). We used the [O III]  $\lambda 5007$  emission line as a template for the  $\lambda 4959$  and H $\beta$  narrow lines. The ratio of [O III]  $\lambda 4959$ /[O III]  $\lambda 5007$  was set at 0.34 (Storey & Zeippen 2000), and Table 10 lists the derived ratios of H $\beta$ /[O III]  $\lambda 5007$ .

The width of the broad H $\beta$  emission line was measured in the narrow-line subtracted mean and rms spectra for each of the objects and is reported as two separate measures: the full width at half-maximum (FWHM) flux and the line dispersion,  $\sigma_{\text{line}}$ , which is the second moment of the emission-line profile (Peterson et al. 2004). The uncertainties in the line widths are set using a Monte Carlo random subset sampling method. In this case, from a set of  $N$  spectra, a random subset of  $N$  spectra is selected without regard to whether a spectrum has previously been chosen and a mean and an rms spectrum are created from the chosen subset. The FWHM and the  $\sigma_{\text{line}}$  are measured and

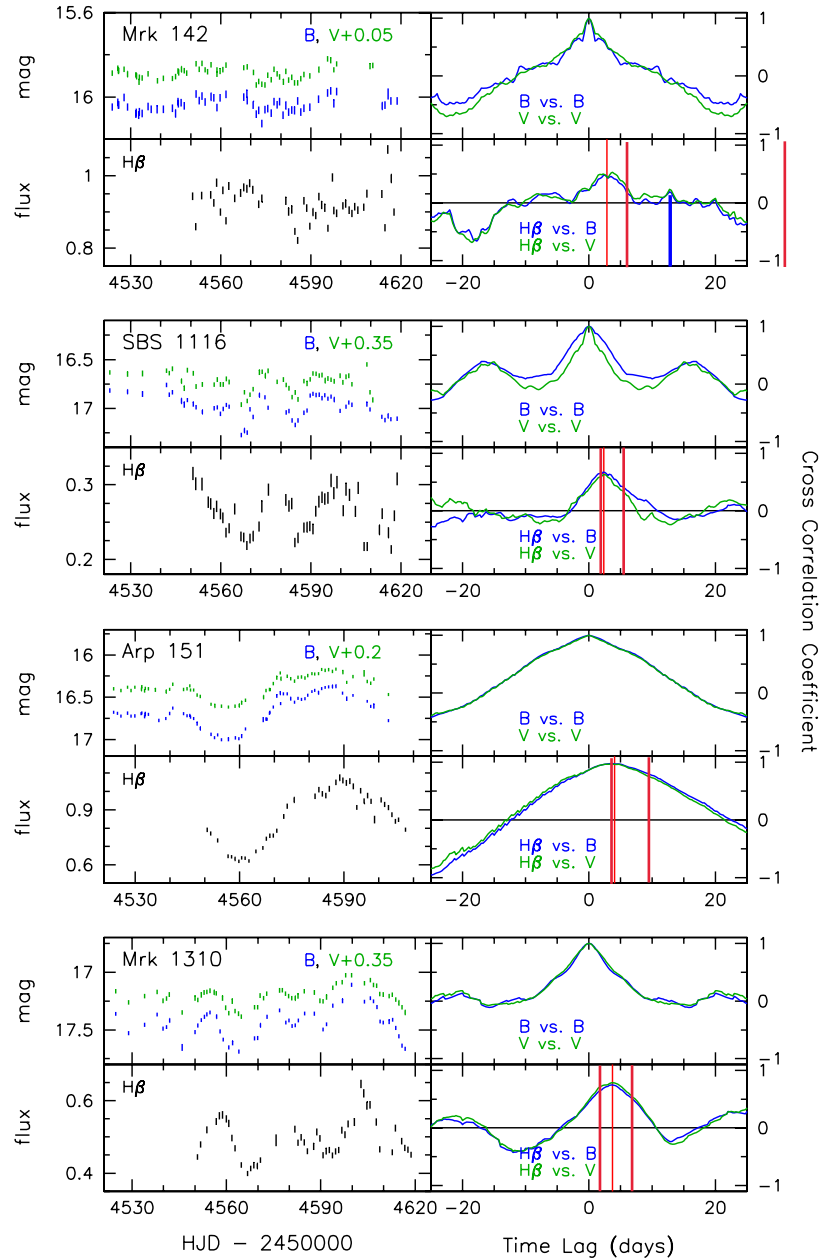


**Figure 1.** Left panels: Photometric and H $\beta$  light curves for Mrk 142, SBS 1116+583A, Arp 151, and Mrk 1310. The photometric measurements have units of Vega magnitudes, and the H $\beta$  emission-line fluxes have units of  $10^{-13}$  erg s $^{-1}$  cm $^{-2}$ . Right panels: Cross-correlation functions for the light curves. For each object, the top panel shows the auto-correlation functions of the photometric light curves and the bottom panel shows the cross-correlation of H $\beta$  with the photometric light curves. The red vertical lines mark the location of the measured lag time (as listed in Table 9) for those objects in which we are able to measure a delay between the continuum and H $\beta$  flux variations.

(A color version of this figure is available in the online journal.)

recorded, and distributions of line-width measurements are built up over 1000 realizations. The mean and standard deviation of each distribution are taken to be the line width and uncertainty, respectively.

In a slight departure from the methods of Peterson et al. (2004), we also attempt to quantify the uncertainty from the exact placement of the continuum. For each object, we define a maximum continuum window (typically 50 Å wide) on either side of the H $\beta$  + [O III] complex. For each realization, a subset of the continuum window on each side of at least 7 pixels (12 Å) is randomly selected, from which the local linear continuum is fit. In general, we find that this additional step does not affect

the uncertainties of the line widths measured in the rms spectra, but slightly increases the errors from measurements made using the mean spectra. This is not particularly surprising, as the mean spectra have much higher S/Ns, so the exact placement of the continuum window defines the specific low-level emission and absorption features from the host-galaxy stellar population that will be included while fitting the continuum. These same low-level features are not detected in an rms spectrum, and the errors are instead dominated by the specifics of which spectra are included.

Finally, we correct the measured line widths for the dispersion of the spectrograph following Peterson et al. (2004). The



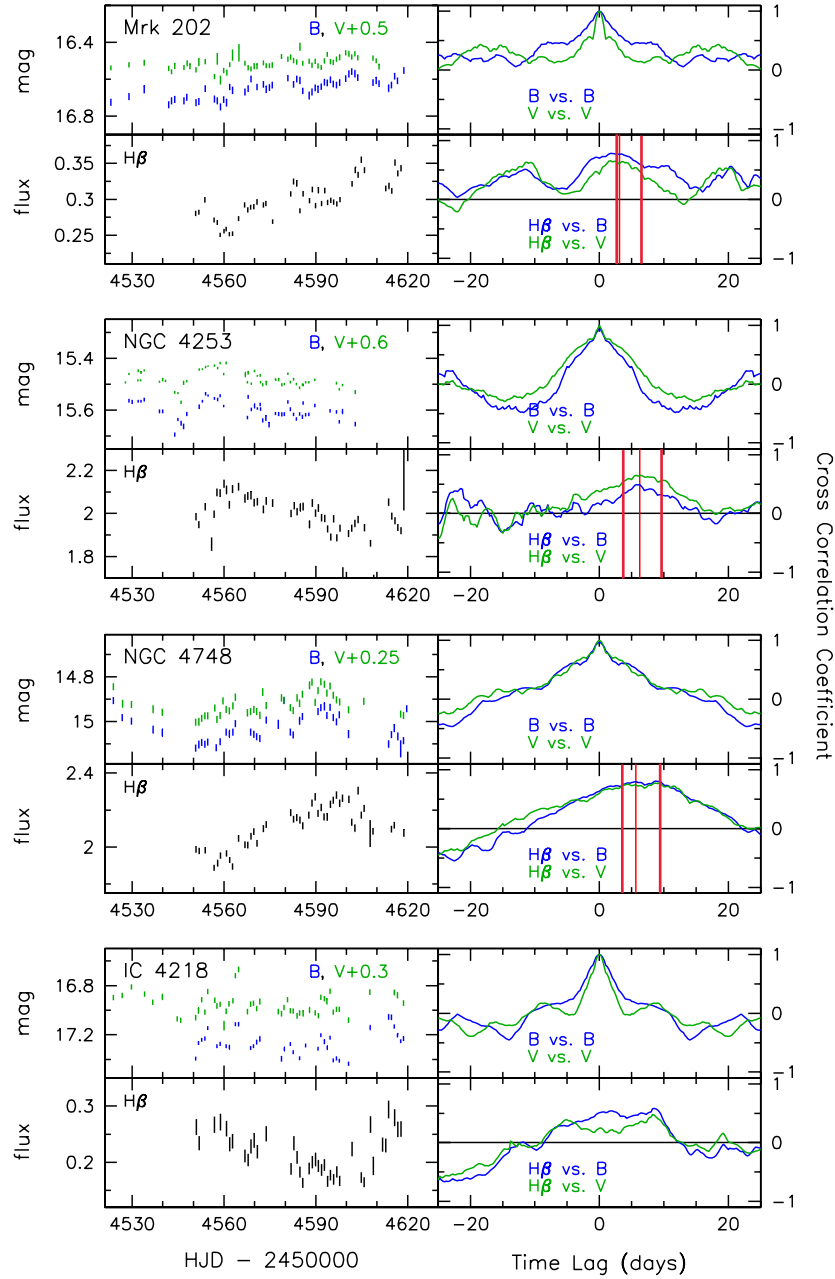


**Figure 2.** Same as Figure 1 for Mrk 202, NGC 4253, NGC 4748, and IC 4218.

(A color version of this figure is available in the online journal.)

observed line width,  $\Delta\lambda_{\text{obs}}$ , can be described as a combination of the intrinsic line width,  $\Delta\lambda_{\text{true}}$ , and the spectrograph dispersion,  $\Delta\lambda_{\text{dis}}$ , such that

$$\Delta\lambda_{\text{obs}}^2 \approx \Delta\lambda_{\text{true}}^2 + \Delta\lambda_{\text{dis}}^2. \quad (2)$$

To measure  $\Delta\lambda_{\text{true}}$ , we take our measurements of the FWHM of [O III]  $\lambda 5007$  as  $\Delta\lambda_{\text{obs}}$ . We then assume that the high-resolution measurements of the widths of [O III]  $\lambda 5007$  for several of the AGNs from Whittle (1992) are  $\Delta\lambda_{\text{true}}$  (listed here in Table 11 after transformation to our adopted units and the observed frame of the galaxy).<sup>21</sup> Given our wide slit width of

<sup>21</sup> The spectroscopic apertures employed in the observations quoted by Whittle (1992) are generally smaller than those employed here; however, narrow-band [O III] imaging of a subset of our sample by Schmitt et al. (2003) shows that the vast majority of the [O III] emission comes from a fairly compact region of  $\sim 1''$  in width.

$4''$  and typical seeing of  $1''$ – $2''$  throughout the campaign, the target AGNs do not fill the entire width of the slit and so we do not measure the dispersion from sky lines or arc lamps (as both of those sources do fill the entire slit width and would bias our dispersion measurement). Given both  $\Delta\lambda_{\text{true}}$  and  $\Delta\lambda_{\text{obs}}$ , we are then able to deduce  $\Delta\lambda_{\text{dis}}$ , the FWHM dispersion of the spectra (also listed in Table 11), which we then use to correct the measurements of the width of the broad H $\beta$  line. For those objects where measurements are not available from Whittle, we assume a FWHM dispersion of  $12.5 \text{ \AA}$ , which is within the range of measured spectral dispersions tabulated in Table 11, but slightly less than the median of  $13.0 \text{ \AA}$  in an attempt to not overcorrect the velocity widths in objects where we do not have a measurement of the intrinsic width of the narrow lines. The slight spread in measured dispersions is a combination of

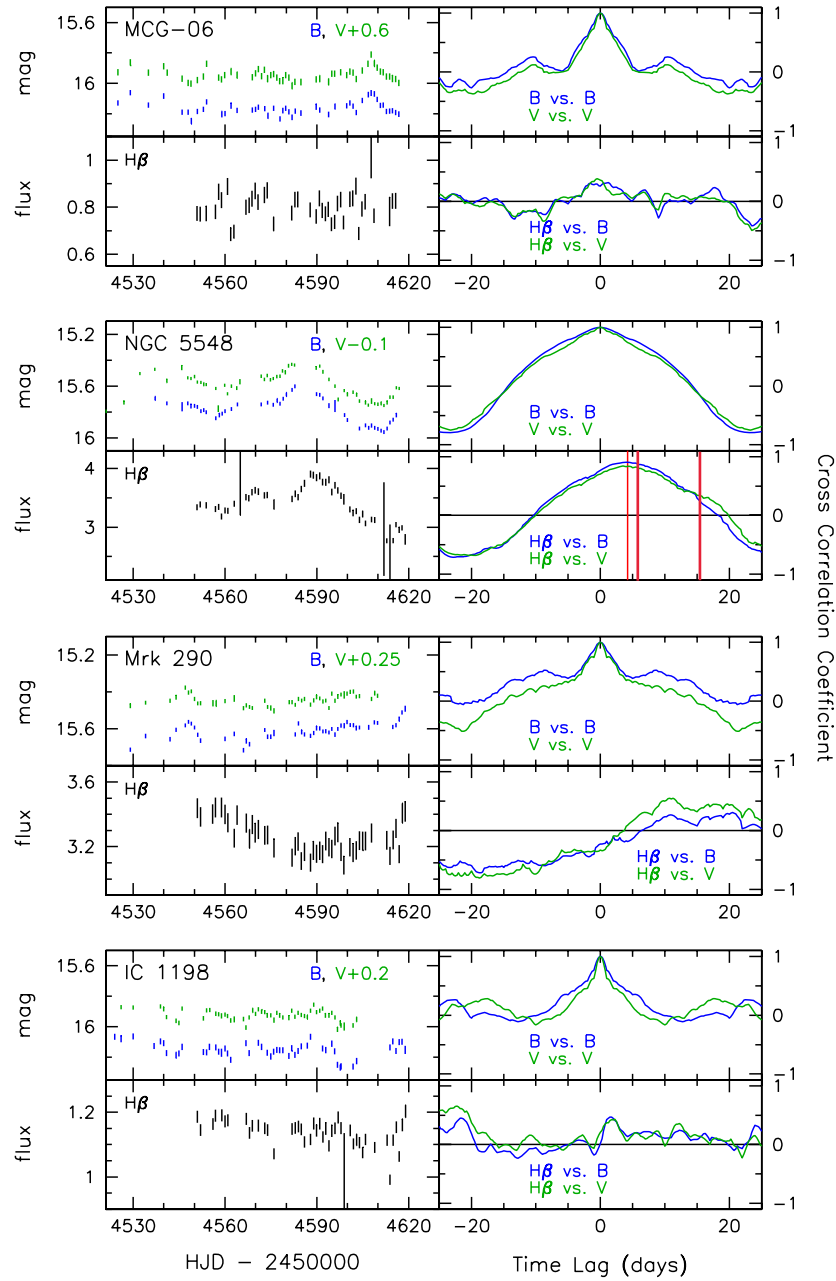


**Figure 3.** Same as Figure 1 for MCG -06-30-15, NGC 5548, Mrk 290, and IC 1198.  
(A color version of this figure is available in the online journal.)

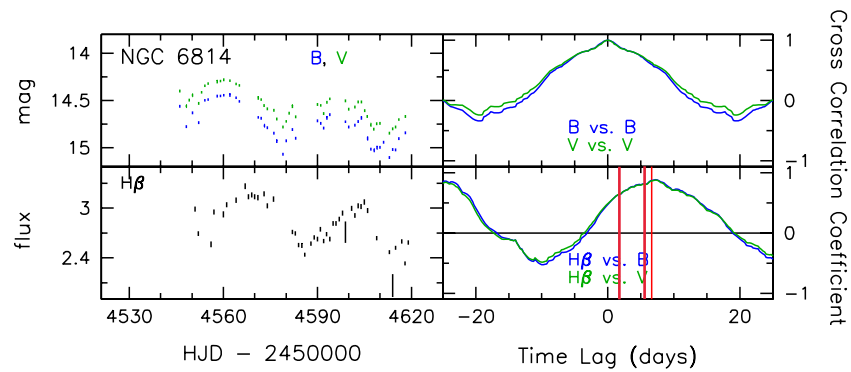


**Figure 4.** Same as Figure 1 for NGC 6814.  
(A color version of this figure is available in the online journal.)

**Table 8**  
Light-curve Statistics

Object (1)	Time Series (2)	$N$ (3)	$\langle T \rangle$ (4)	$T_{\text{median}}$ (5)	$\langle \sigma_f / f \rangle$ (6)	$F_{\text{var}}$ (7)	$R_{\text{max}}$ (8)
Mrk 142	$B$	64	$1.8 \pm 2.3$	1.02	0.0166	0.025	$1.15 \pm 0.03$
	$V$	62	$1.7 \pm 2.0$	1.02	0.0119	0.024	$1.12 \pm 0.02$
	5100 Å	51	$1.4 \pm 1.0$	1.00	0.0115	0.090	$1.86 \pm 0.03$
	H $\beta$	51	$1.4 \pm 1.0$	1.00	0.0113	0.086	$1.97 \pm 0.03$
SBS 1116+583A	$B$	56	$2.1 \pm 1.8$	1.02	0.0205	0.104	$1.63 \pm 0.05$
	$V$	56	$1.9 \pm 1.7$	1.01	0.0220	0.082	$1.47 \pm 0.05$
	5100 Å	50	$1.4 \pm 0.9$	1.00	0.0437	0.043	$1.36 \pm 0.08$
	H $\beta$	50	$1.4 \pm 0.9$	1.00	0.0279	0.102	$1.48 \pm 0.06$
Arp 151	$B$	66	$1.5 \pm 1.6$	1.02	0.0173	0.161	$1.80 \pm 0.04$
	$V$	62	$1.6 \pm 1.6$	1.02	0.0185	0.113	$1.54 \pm 0.04$
	5100 Å	43	$1.4 \pm 1.9$	1.02	0.0101	0.120	$1.73 \pm 0.03$
	H $\beta$	43	$1.4 \pm 1.9$	1.02	0.0153	0.169	$1.74 \pm 0.04$
Mrk 1310	$B$	50	$2.0 \pm 1.5$	1.16	0.0160	0.116	$1.71 \pm 0.04$
	$V$	58	$1.8 \pm 1.4$	1.05	0.0183	0.073	$1.39 \pm 0.04$
	5100 Å	47	$1.5 \pm 1.1$	1.01	0.0367	0.051	$1.44 \pm 0.07$
	H $\beta$	47	$1.5 \pm 1.1$	1.01	0.0186	0.108	$1.62 \pm 0.04$
Mrk 202	$B$	58	$2.0 \pm 1.7$	1.01	0.0168	0.042	$1.20 \pm 0.03$
	$V$	58	$1.8 \pm 1.7$	1.01	0.0143	0.027	$1.18 \pm 0.04$
	5100 Å	46	$1.5 \pm 1.2$	1.01	0.0309	0.027	$1.25 \pm 0.05$
	H $\beta$	46	$1.5 \pm 1.2$	1.01	0.0125	0.089	$1.42 \pm 0.03$
NGC 4253	$B$	51	$1.9 \pm 2.3$	1.02	0.0066	0.032	$1.16 \pm 0.01$
	$V$	54	$1.8 \pm 2.2$	1.01	0.0046	0.028	$1.15 \pm 0.01$
	5100 Å	50	$1.4 \pm 1.0$	1.01	0.0180	0.053	$1.31 \pm 0.03$
	H $\beta$	50	$1.4 \pm 1.0$	1.01	0.0116	0.048	$1.35 \pm 0.15$
NGC 4748	$B$	48	$2.4 \pm 3.1$	1.25	0.0151	0.053	$1.22 \pm 0.05$
	$V$	52	$2.2 \pm 2.5$	1.03	0.0147	0.043	$1.18 \pm 0.02$
	5100 Å	45	$1.5 \pm 1.3$	1.00	0.0202	0.045	$1.33 \pm 0.04$
	H $\beta$	45	$1.5 \pm 1.3$	1.00	0.0094	0.052	$1.22 \pm 0.02$
IC 4218	$B$	42	$2.8 \pm 5.5$	1.03	0.0154	0.087	$1.42 \pm 0.04$
	$V$	65	$2.1 \pm 1.9$	1.09	0.0203	0.079	$1.52 \pm 0.06$
	5100 Å	40	$1.7 \pm 1.5$	1.00	0.0731	0.077	$1.85 \pm 0.19$
	H $\beta$	40	$1.7 \pm 1.5$	1.00	0.0551	0.159	$1.90 \pm 0.14$
MCG −06-30-15	$B$	48	$2.1 \pm 1.7$	1.08	0.0165	0.037	$1.19 \pm 0.03$
	$V$	55	$1.9 \pm 1.6$	1.04	0.0192	0.032	$1.21 \pm 0.03$
	5100 Å	42	$1.6 \pm 1.2$	1.00	0.0849	0.106	$1.66 \pm 0.20$
	H $\beta$	42	$1.6 \pm 1.2$	1.00	0.0442	0.067	$1.61 \pm 0.26$
NGC 5548	$B$	45	$2.4 \pm 4.3$	1.07	0.0148	0.085	$1.39 \pm 0.03$
	$V$	57	$1.9 \pm 1.8$	1.05	0.0125	0.094	$1.40 \pm 0.02$
	5100 Å	51	$1.4 \pm 0.9$	1.01	0.0216	0.058	$1.32 \pm 0.04$
	H $\beta$	51	$1.4 \pm 0.9$	1.01	0.0279	0.082	$1.57 \pm 0.35$
Mrk 290	$B$	50	$2.3 \pm 2.8$	1.01	0.0107	0.038	$1.23 \pm 0.02$
	$V$	50	$2.1 \pm 2.5$	1.01	0.0107	0.024	$1.12 \pm 0.02$
	5100 Å	48	$1.5 \pm 1.1$	1.01	0.0169	0.031	$1.19 \pm 0.03$
	H $\beta$	48	$1.5 \pm 1.1$	1.01	0.0178	0.025	$1.12 \pm 0.03$
IC 1198	$B$	55	$2.0 \pm 2.0$	1.05	0.0185	0.039	$1.21 \pm 0.03$
	$V$	58	$1.6 \pm 1.7$	1.02	0.0134	0.031	$1.16 \pm 0.02$
	5100 Å	45	$1.5 \pm 1.2$	1.01	0.0300	0.054	$1.36 \pm 0.06$
	H $\beta$	45	$1.5 \pm 1.2$	1.01	0.0187	0.031	$1.22 \pm 0.18$
NGC 6814	$B$	43	$1.7 \pm 1.3$	1.04	0.0137	0.178	$1.83 \pm 0.03$
	$V$	46	$1.6 \pm 1.3$	1.02	0.0134	0.145	$1.68 \pm 0.03$
	5100 Å	45	$1.5 \pm 1.1$	1.01	0.0345	0.068	$1.54 \pm 0.08$
	H $\beta$	45	$1.5 \pm 1.1$	1.01	0.0124	0.093	$1.58 \pm 0.11$

**Notes.** Columns are presented as follows: (1) object; (2) feature; (3) number of observations; (4) average interval between observations in days; (5) median sampling rate in days; (6) mean fractional error; (7) excess variance as described in the text; and (8) ratio of the maximum to the minimum flux.

factors including seeing, guiding, and the angular size of the narrow-line region in each object.

We list the rest-frame, dispersion-corrected broad H $\beta$  line width measurements in Table 12, from the mean and the rms spectra of each of the nine objects with significant H $\beta$  lag signatures. The average ratio of H $\beta$  line widths measured in the mean spectra to those in the rms spectra is  $1.4 \pm 0.3$  for

$\sigma_{\text{line}}$  and  $1.3 \pm 0.7$  ( $1.2 \pm 0.2$  excluding NGC 4748) for FWHM. The average ratio of FWHM/ $\sigma_{\text{line}}$  is  $1.89 \pm 0.07$  in the mean spectra and  $2.0 \pm 1.1$  ( $2.1 \pm 0.5$  excluding NGC 4748) in the rms spectra. This is consistent with the findings of Collin et al. (2006) that AGNs with narrow broad-line components (i.e.,  $\sigma_{\text{line}} < 2000 \text{ km s}^{-1}$ ) have ratios of FWHM/ $\sigma_{\text{line}}$  that are less than the expected value for a Gaussian line profile

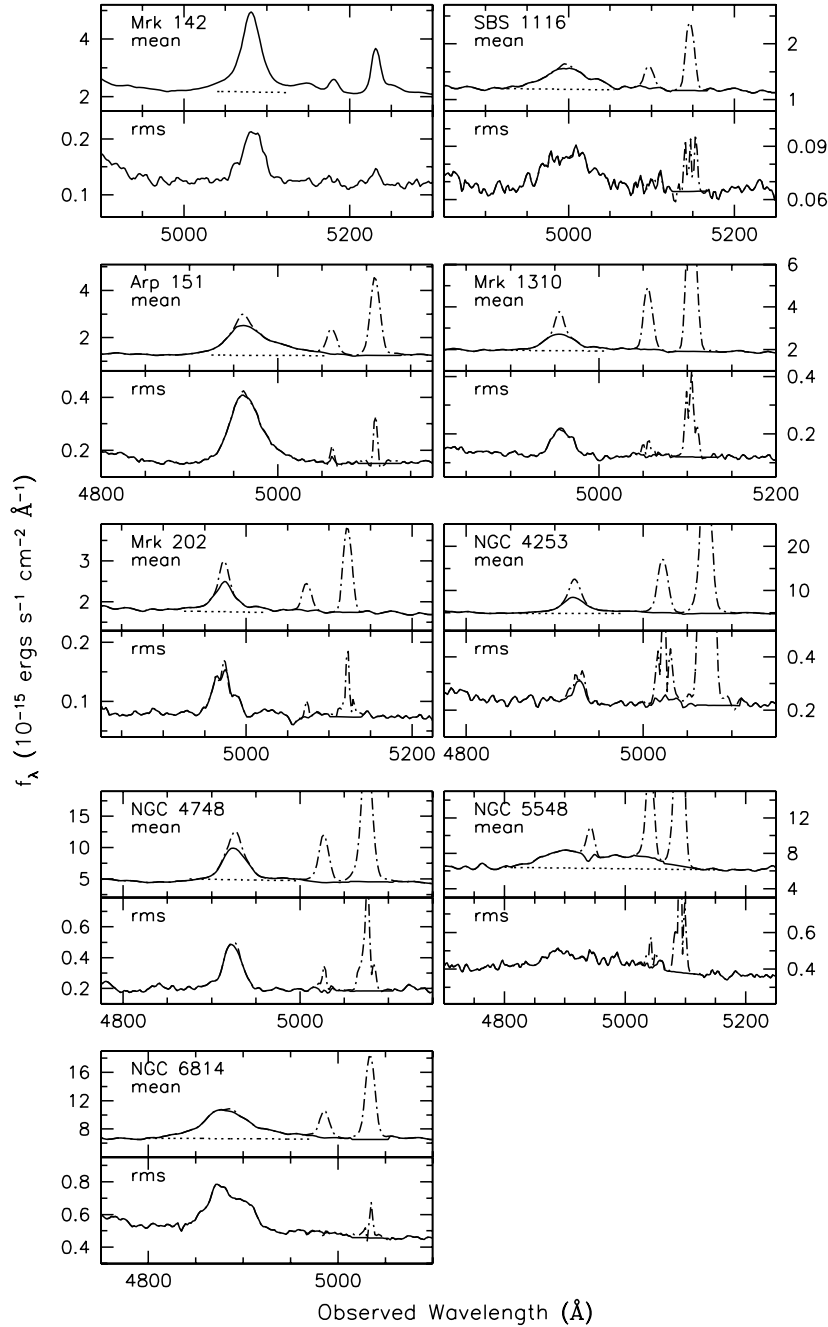


**Figure 5.** Mean and variable (rms) spectra of the AGNs. The solid lines are the narrow-line subtracted spectra, while the dot-dashed lines show the contributions from the H $\beta$  and [O III]  $\lambda\lambda 4959, 5007$  narrow lines. The dotted lines under the mean H $\beta$  profiles show the interpolated continuum level for each object.

of 2.35. It is also worth noting that NGC 5548, which had a very broad H $\beta$  line width during the monitoring campaign ( $\sigma_{\text{line}} > 2000 \text{ km s}^{-1}$ ) has ratios of  $\text{FWHM}/\sigma_{\text{line}} > 2.35$  in both the mean and rms spectra.

### 3.3. Black Hole Mass

Determination of black hole masses from reverberation mapping rests upon the assumption that the gravity of the central, supermassive black hole dominates the motions of the gas in the BLR. The existence of a “virial” relationship between time lag and line width,  $v \propto \tau^{-0.5}$ , has been clearly shown in NGC 5548 (Peterson & Wandel 1999), and has been seen in many other objects (Peterson et al. 2000; Onken & Peterson 2002; Kollatschny 2003) upholding this basic assumption.

The black hole mass is determined via the virial equation

$$M_{\text{BH}} = f \frac{c\tau v^2}{G}, \quad (3)$$

where  $\tau$  is the mean time delay for the region of interest (here, the H $\beta$ -emitting region),  $v$  is the velocity of gas in that region,  $c$  is the speed of light,  $G$  is the gravitational constant, and  $f$  is a scaling factor of order unity that depends on the detailed geometry and kinematics of the line-emitting region.

Peterson et al. (2004) demonstrate that the combination of  $\tau_{\text{cent}}$  and  $\sigma_{\text{line,rms}}$  provides the most robust measurement of the black hole mass. By comparing the resultant masses derived from several emission lines and independent data sets for the same objects, the combination of  $\tau_{\text{cent}}$  and  $\sigma_{\text{line,rms}}$  results in



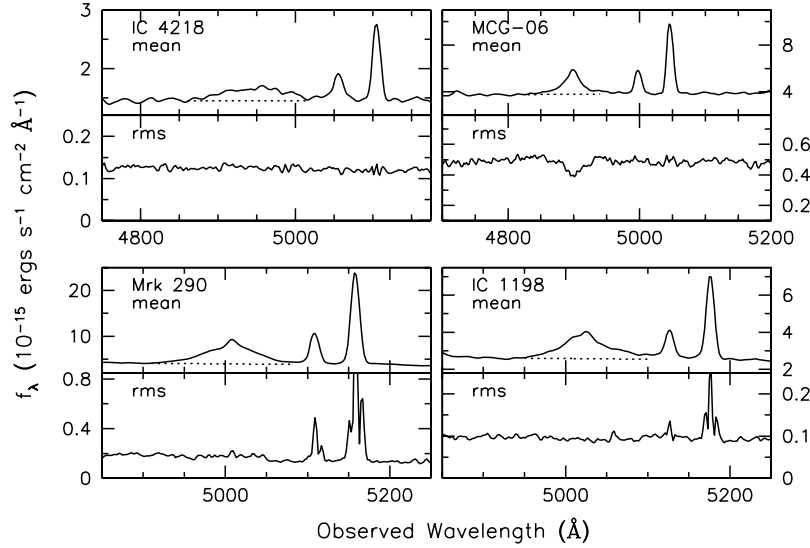


**Figure 6.** Mean and rms spectra of the AGNs without strong variability: IC 4218, MCG -06-30-15, Mrk 290, and IC 1198. The poor seeing at high air mass ( $\sec z > 3$ ) and a nearby bright star caused the continuum variations in the spectra of MCG -06-30-15 to be stronger than the H $\beta$  variations, causing the apparent inverted structure in the rms spectrum of this object.

**Table 9**  
H $\beta$  Time Lag Measurements

Object	Observed		Rest frame	
	$\tau_{\text{cent}}$ (days)	$\tau_{\text{peak}}$ (days)	$\tau_{\text{cent}}$ (days)	$\tau_{\text{peak}}$ (days)
vs. <i>B</i> band				
Mrk 142	$2.87^{+0.76}_{-0.87}$	$2.75^{+1.00}_{-0.75}$	$2.74^{+0.73}_{-0.83}$	$2.63^{+0.96}_{-0.72}$
SBS 1116+583A	$2.38^{+0.64}_{-0.51}$	$2.25^{+1.00}_{-0.50}$	$2.31^{+0.62}_{-0.49}$	$2.19^{+0.97}_{-0.49}$
Arp 151	$4.08^{+0.50}_{-0.69}$	$3.50^{+0.75}_{-0.25}$	$3.99^{+0.49}_{-0.68}$	$3.43^{+0.73}_{-0.24}$
Mrk 1310	$3.74^{+0.60}_{-0.62}$	$3.75^{+0.50}_{-0.50}$	$3.66^{+0.59}_{-0.61}$	$3.68^{+0.49}_{-0.49}$
Mrk 202	$3.12^{+1.77}_{-1.15}$	$3.00^{+1.50}_{-1.25}$	$3.05^{+1.73}_{-1.12}$	$2.94^{+1.47}_{-1.22}$
NGC 4253	$6.24^{+1.65}_{-1.24}$	$6.00^{+2.50}_{-1.00}$	$6.16^{+1.63}_{-1.22}$	$5.92^{+2.47}_{-0.99}$
NGC 4748	$5.63^{+1.64}_{-2.25}$	$5.75^{+3.50}_{-2.00}$	$5.55^{+1.62}_{-2.22}$	$5.67^{+3.45}_{-1.97}$
NGC 5548	$4.25^{+0.88}_{-1.33}$	$4.25^{+1.25}_{-1.50}$	$4.18^{+0.86}_{-1.30}$	$4.18^{+1.23}_{-1.47}$
NGC 6814	$6.67^{+0.88}_{-0.90}$	$7.25^{+0.25}_{-0.75}$	$6.64^{+0.87}_{-0.90}$	$7.21^{+0.25}_{-0.75}$
vs. <i>V</i> band				
Mrk 142	$2.88^{+1.00}_{-1.01}$	$3.25^{+0.75}_{-1.75}$	$2.76^{+0.96}_{-0.96}$	$3.11^{+0.72}_{-1.67}$
SBS 1116+583A	$2.24^{+0.65}_{-0.61}$	$2.25^{+0.75}_{-0.50}$	$2.18^{+0.63}_{-0.60}$	$2.19^{+0.73}_{-0.49}$
Arp 151	$3.52^{+0.82}_{-0.72}$	$3.50^{+1.00}_{-0.75}$	$3.45^{+0.80}_{-0.71}$	$3.43^{+0.98}_{-0.73}$
Mrk 1310	$3.67^{+0.46}_{-0.50}$	$3.75^{+0.50}_{-0.50}$	$3.60^{+0.45}_{-0.49}$	$3.68^{+0.49}_{-0.49}$
Mrk 202	$3.11^{+0.91}_{-1.12}$	$2.75^{+1.75}_{-1.25}$	$3.05^{+0.89}_{-1.10}$	$2.69^{+1.71}_{-1.22}$
NGC 4253	$6.87^{+1.22}_{-1.84}$	$6.50^{+2.25}_{-2.00}$	$6.78^{+1.20}_{-1.81}$	$6.42^{+2.22}_{-1.97}$
NGC 4748	$6.39^{+1.84}_{-1.46}$	$7.75^{+1.75}_{-3.75}$	$6.30^{+1.82}_{-1.44}$	$7.64^{+1.72}_{-3.70}$
NGC 5548	$4.24^{+0.91}_{-1.35}$	$4.25^{+1.50}_{-1.25}$	$4.17^{+0.90}_{-1.33}$	$4.18^{+1.47}_{-1.23}$
NGC 6814	$6.49^{+0.95}_{-0.96}$	$7.00^{+0.50}_{-0.50}$	$6.46^{+0.94}_{-0.96}$	$6.96^{+0.50}_{-0.50}$

**Table 10**  
H $\beta$  Narrow-component Strength

Object	$f(\text{H}\beta)/f([\text{O III}] \lambda 5007)$	Ref.
Mrk 142	0.274	1
SBS 1116+583A	0.07	2
Arp 151	0.15	2
Mrk 1310	0.13	2
Mrk 202	0.30	2
NGC 4253	0.113	1
NGC 4748	0.15	2
NGC 5548	0.114	1
NGC 6814	0.03	2

**References.** (1) Marziani et al. 2003; (2) this work.

**Table 11**  
[O III]  $\lambda 5007$  Line Widths and Spectral Dispersion

Object	FWHM ([O III] $\lambda 5007$ ) <sup>a</sup> (km s <sup>-1</sup> )	FWHM (observed) (Å)	$\Delta\lambda_{\text{dis}}$ (Å)
Arp 151	220	$13.583 \pm 0.013$	13.1
Mrk 1310	120	$12.565 \pm 0.013$	12.4
NGC 4253	180	$14.955 \pm 0.013$	14.6
NGC 5548	410	$16.521 \pm 0.010$	14.7
Mrk 290	380	$13.319 \pm 0.009$	11.6
IC 1198	280	$12.971 \pm 0.003$	12.0
NGC 6814	125	$13.021 \pm 0.008$	12.9

**Note.** <sup>a</sup> Line widths are from Whittle (1992).

the least amount of scatter in the resultant masses of all the combinations possible between the various line width and lag time measures. For the derived black hole masses presented here, we will therefore adopt the combination of  $\tau_{\text{cent}}$  and  $\sigma_{\text{line,rms}}$ .

The absolute scaling of reverberation masses, the  $f$  factor in Equation (3), is currently unknown. Rather than assuming a specific value of  $f$  (e.g., Netzer 1990), and therefore assuming specific physical details of the BLR, we instead adopt the scaling factor determined by Onken et al. (2004) of  $\langle f \rangle \approx 5.5$ . This is the average value required to bring the  $M_{\text{BH}}-\sigma_*$  relationship

for reverberation-mapped AGNs into agreement with the  $M_{\text{BH}}-\sigma_*$  relationship determined for local, quiescent galaxies with dynamical mass measurements.

Table 13 lists the black hole masses for the nine objects presented in this work with H $\beta$  reverberation signals. We list both the “virial product,” which assumes that  $f = 1$ , as well as the adopted black hole mass using the Onken et al. (2004) scaling factor. Figure 7 shows the range of black hole masses currently probed by reverberation mapping. The new masses determined here (solid histogram, not including NGC 5548) lie primarily in the range  $10^6$ – $10^7 M_{\odot}$ , in agreement with the expectations from

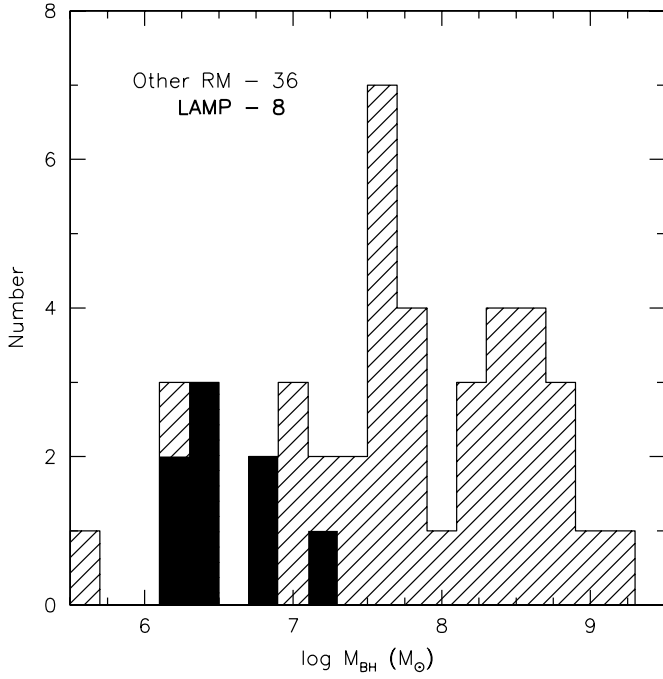


**Figure 7.** Range of black hole masses currently probed by reverberation-mapping experiments. The 36 black hole masses that make up the hashed histogram come from Peterson et al. (2004, 2005) and updates since then by Bentz et al. (2006b, 2007); Denney et al. (2006, 2009), and Grier et al. (2008). The eight new masses derived from the results presented here make up the solid histogram and primarily lie between  $10^6$  and  $10^7 M_\odot$ .

**Table 12**  
Rest-frame Broad H $\beta$  Line-width Measurements

Object	Mean Spectrum		rms Spectrum	
	$\sigma_{\text{line}}$ (km s $^{-1}$ )	FWHM (km s $^{-1}$ )	$\sigma_{\text{line}}$ (km s $^{-1}$ )	FWHM (km s $^{-1}$ )
Mrk 142	1116 $\pm$ 22	1462 $\pm$ 2	859 $\pm$ 102	1368 $\pm$ 379
SBS 1116+583A	1552 $\pm$ 36	3668 $\pm$ 186	1528 $\pm$ 184	3604 $\pm$ 1123
Arp 151	2006 $\pm$ 24	3098 $\pm$ 69	1252 $\pm$ 46	2357 $\pm$ 142
Mrk 1310	1209 $\pm$ 42	2409 $\pm$ 24	755 $\pm$ 138	1602 $\pm$ 250
Mrk 202	867 $\pm$ 40	1471 $\pm$ 18	659 $\pm$ 65	1354 $\pm$ 250
NGC 4253	1088 $\pm$ 37	1609 $\pm$ 39	516 $\pm$ 218	834 $\pm$ 1260
NGC 4748	1009 $\pm$ 27	1947 $\pm$ 66	657 $\pm$ 91	1212 $\pm$ 173
NGC 5548	4266 $\pm$ 65	12771 $\pm$ 71	4270 $\pm$ 292	11177 $\pm$ 2266
NGC 6814	1918 $\pm$ 36	3323 $\pm$ 7	1610 $\pm$ 108	3277 $\pm$ 297

single-epoch estimates, and extending the range of black hole mass coverage by a factor of  $\sim 10$ .

### 3.4. NGC 5548: The Control Object

NGC 5548 has by far the most independent reverberation-mapping data sets of any individual AGN. As a result, there is known to exist a “virial” relationship between the broad-line width and the lag time, which strongly suggests that the motion of the gas in the BLR is dominated by a central supermassive object (Peterson & Wandel 1999). Figure 8 shows this relationship for all of the independent H $\beta$  reverberation results for NGC 5548, as well as the relationship for all broad emission lines, including C IV, C III, and H $\alpha$ . The open circles are the results from previous reverberation-mapping campaigns, and the filled circle shows the measurements of  $\tau_{\text{cent}}$  and  $\sigma_{\text{line}}$  for H $\beta$  presented here. The H $\beta$  time lag presented here is the shortest H $\beta$  lag measured for NGC 5548, and is one of the shortest lags measured for any emission line in NGC 5548.

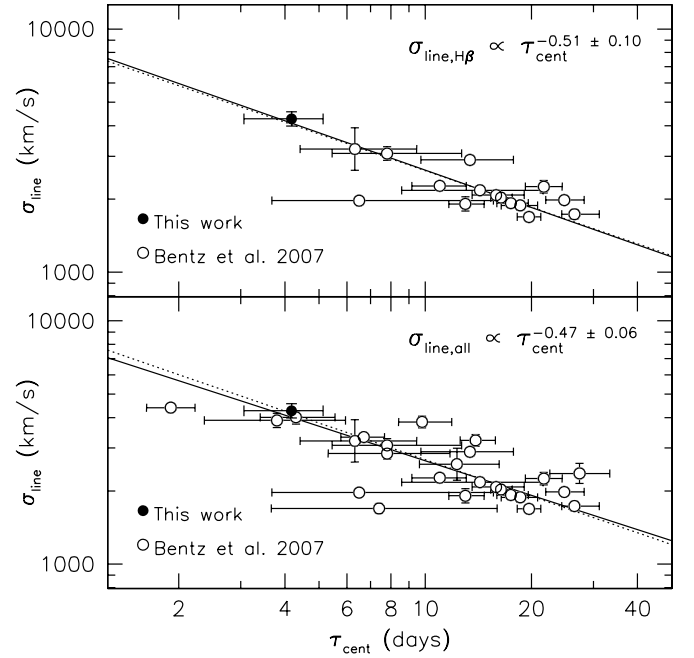


**Figure 8.** Relationship between lag time and line width for several independent reverberation studies of NGC 5548. The top panel shows the relationship for H $\beta$  reverberation results only, while the bottom panel shows the relationship for all broad emission lines with reverberation results. The dark circle in each panel is the H $\beta$  result from this work, while the open circles are the compilation of results from Bentz et al. (2007) and references therein. The solid lines show the best fits to the relationship, with the slopes noted in each panel. The dotted lines show the relationship with the slope fixed at the value expected for a virial relationship, i.e.,  $-0.5$ .

**Table 13**  
Virial Products and Derived Black Hole Masses

Object	$c\tau_{\text{cent}}\sigma_{\text{line}}^2/G$ ( $10^6 M_\odot$ )	$M_{\text{BH}}^a$ ( $10^6 M_\odot$ )
Mrk 142	0.40 $^{+0.14}_{-0.15}$	2.17 $^{+0.77}_{-0.83}$
SBS 1116+583A	1.05 $^{+0.38}_{-0.34}$	5.80 $^{+2.09}_{-1.86}$
Arp 151	1.22 $^{+0.17}_{-0.23}$	6.72 $^{+0.96}_{-1.24}$
Mrk 1310	0.41 $^{+0.16}_{-0.16}$	2.24 $^{+0.90}_{-0.90}$
Mrk 202	0.26 $^{+0.16}_{-0.11}$	1.42 $^{+0.85}_{-0.59}$
NGC 4253	0.32 $^{+0.28}_{-0.25}$	1.76 $^{+1.56}_{-1.40}$
NGC 4748	0.47 $^{+0.19}_{-0.23}$	2.57 $^{+1.03}_{-1.25}$
NGC 5548	14.9 $^{+3.7}_{-5.1}$	82 $^{+20}_{-28}$
NGC 6814	3.36 $^{+0.63}_{-0.64}$	18.5 $^{+3.5}_{-3.5}$

**Note.** <sup>a</sup> Assuming  $f = 5.5$ .

NGC 5548 has been in a very low luminosity state for the past several years (see Bentz et al. 2007), and its current luminosity<sup>22</sup> of  $\lambda L_\lambda(5100\text{\AA}) = 8.7 \times 10^{42} \text{ erg s}^{-1}$  is only  $\sim 20\%$  brighter than its lowest observed luminosity state in Spring 2005. The low luminosity of the AGN has resulted in a very broad, low-level, double-peaked H $\beta$  emission-line profile in NGC 5548, which does increase the difficulty of accurately measuring the line width. Despite this, the combination of lag time and line width measured here falls where it is expected in Figure 8.

Additionally, we can compare the individual virial products for NGC 5548 as determined from each H $\beta$  reverberation data

<sup>22</sup> The luminosity at rest frame 5100  $\text{\AA}$  has been corrected for the contribution from starlight using *Hubble Space Telescope* (HST) imaging and the method of Bentz et al. (2006a, 2009a).

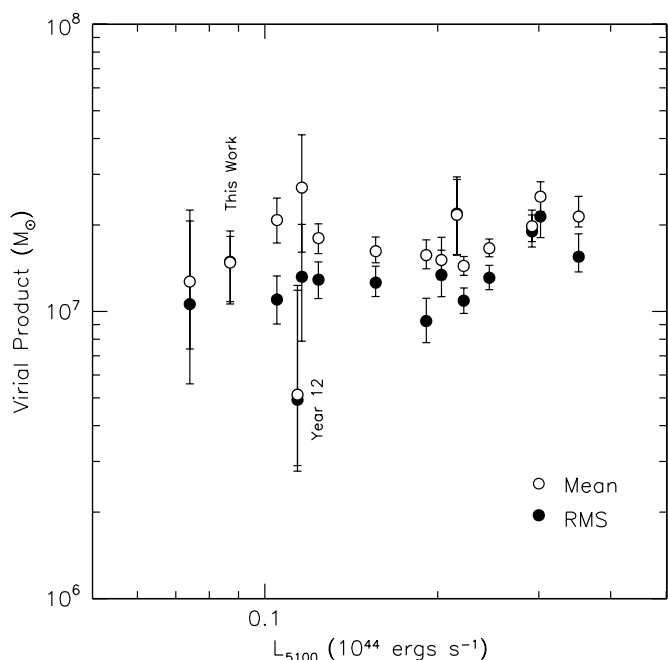


**Figure 9.** Relationship between optical AGN luminosity and derived virial product for NGC 5548. The open circles show the virial product based on  $\sigma_{\text{line}}$  measured from the mean spectrum, and the filled circles are based on  $\sigma_{\text{line}}$  measured from the rms spectrum.

set. Figure 9 shows the virial product as a function of AGN luminosity, with open circles representing the virial product based on  $\sigma_{\text{line}}$  as measured in the mean spectrum, and filled circles with  $\sigma_{\text{line}}$  from the rms spectrum. While similar to Figure 7 of Bentz et al. (2007), the luminosities have been updated with the new host-galaxy corrections of Bentz et al. (2009a). The point denoted as “Year 12” is the monitoring data set from the year 2000 and is known to be very poorly sampled and to yield ambiguous results when the  $H\beta$  light curve is cross-correlated with the continuum light curve (Peterson et al. 2002).

The virial products from the time lag and line widths presented here are consistent with previous results within the observed scatter. There does not seem to be any significant trend over  $\sim 0.6$  dex in AGN luminosity, meaning that the resultant virial product is not dependent on the luminosity state of the AGN.

The agreement between the results for NGC 5548 presented here and the results from the previous 14 independent reverberation-mapping experiments for this same object shows that reverberation mapping is both repeatable and reliable. This agreement also shows that there are no systematic biases in the LAMP analysis that would otherwise be absent from similar high-quality reverberation-mapping experiments.

#### 4. VELOCITY-RESOLVED TIME LAGS

Up to this point, the discussion of the reverberation response for the objects in the LAMP sample has centered around the average time lag for the broad emission variability, which is related to the average size of the  $H\beta$ -emitting BLR. However, the average time lag is simply the first moment of the so-called “transfer function,” which describes the detailed line response as a function of time and velocity (see Peterson 2001 for a full review).

To illustrate a sample of possible expected transfer function behaviors, Figure 10 shows model transfer functions for three different kinematic states of the BLR: (a) circular Keplerian orbits with isotropic orientations, (b) gravitational free-falling inflow, and (c) a constantly accelerated outflow. The BLR geometry and radiation parameters are the same for each model: the emission is restricted to a biconical structure with a semi-opening angle of  $30^\circ$  and an inclination of  $20^\circ$ , such that the observer is inside the beam. The line emission is enhanced for clouds at smaller radii, and is partially anisotropic with enhanced radiation in the direction of the source. Each resulting model is a physically motivated and relatively plausible, although likely simplified, model of an AGN BLR (for additional models, see e.g., Welsh & Horne 1991; Horne et al. 2004). While the details of the transfer function and emission-line profile depend on the exact geometry and line emission mechanics in the model, the

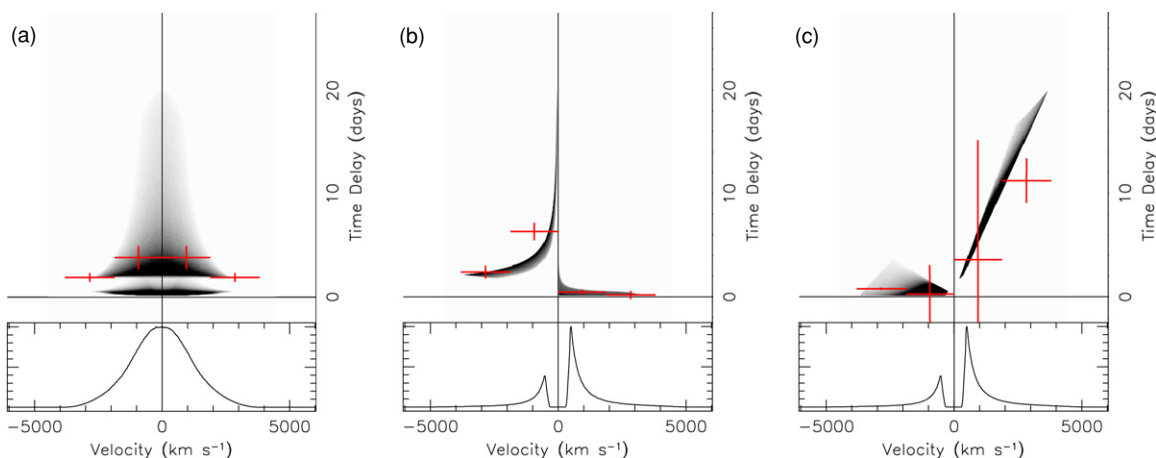


**Figure 10.** Model transfer functions for broad-line regions with simple kinematics of (a) circular Keplerian orbits with isotropic orientations, (b) gravitational free-fall inflow, and (c) outflow with a constant acceleration (i.e., a Hubble or ballistic outflow). The gray-scale images show the full two-dimensional structure, while the vertical red error bars show the weighted mean and standard deviation of the time lag within discrete velocity bins that are represented by the horizontal red error bars. For each of the three kinematic examples, the bottom panel shows the expected line profile (i.e., the two-dimensional structure integrated over all lag times). For each of the models, the line emission is restricted to a bicone with a semi-opening angle of  $30^\circ$  and the model is inclined at  $20^\circ$  so that the observer is inside the beam. The radiation structure within the BLR clouds is set so that the emission is enhanced for clouds at smaller radii, and the line emission is partially anisotropic, such that the emission is enhanced in the direction of the illuminating source. The overall behavior of the red points is different for each of the three models: a symmetric structure around zero velocity for circular Keplerian orbits, longer lags in the blueshifted emission for inflow, and longer lags in the redshifted emission for outflow.

(A color version of this figure is available in the online journal.)

overall behavior for each kinematic state does not really change: BLR clouds with circular orbits produce a symmetric response around zero velocity, while inflow produces longer lag times in the blueshifted emission and outflow produces the opposite, or longer lags in the redshifted emission. Therefore, recovery of the transfer function can be an extremely powerful tool for discriminating between plausible models for the BLR and is, in fact, the immediate goal of reverberation-mapping experiments.

However, achieving this goal is technically and observationally challenging. Several techniques have been developed in an attempt to grapple with the technical difficulties, including the maximum entropy method (MEM; Horne 1994), subtractively optimized local averages (Pijpers & Wanders 1994), and regularized linear inversion (Krolik & Done 1995). Reverberation data sets are limited in sampling duration and generally irregularly sampled, which, coupled with flux uncertainties that are usually only a factor of a few smaller than the flux variability amplitude, has placed severe limitations on past attempts at transfer function recovery. A partially recovered transfer function for the C IV–He II region of NGC 4151 was hampered by extremely strong absorption in the C IV line core, but perhaps shows some evidence for radial infall (Ulrich & Horne 1996). Kollatschny (2003) explored the behavior of several optical emission lines in the spectrum of Mrk 110 and found possible indications for radial outflow. Unfortunately, these and the few other published attempts in the past have yielded notoriously ambiguous results, a fact which is best illustrated by the analyses of the *HST* C IV data set for NGC 5548 by several independent groups. Each of the studies concluded by favoring a different and conflicting model of the C IV emitting gas in the BLR of NGC 5548: no radial motion (Wanders et al. 1995), some radial infall (Done & Krolik 1996), and radial outflow (Chiang & Murray 1996; Bottorff et al. 1997), and all of these conclusions were based on analysis of the *same data*.

Failure to achieve the goal of recovering a full, unambiguous transfer function has led to more stringent observational requirements for reverberation-mapping experiments, including higher and more regular sampling rates, longer sampling durations, and higher spectral resolution and S/N requirements for each of the individual spectra (e.g., Horne et al. 2004). All of these requirements were carefully considered while planning the LAMP observations, although past difficulties and the relatively low luminosities of the target AGNs did not immediately promote transfer function recovery as a main goal of this project. Because a full analysis of the reverberation data presented here using the MEM or other techniques is beyond the scope of this paper, we instead investigated whether there appeared to be any strong signals of velocity-resolved time lag information in the LAMP data sets. For the six objects with the clearest average time lag signatures, we measured the average lag time as a function of velocity by creating light curves from the H $\beta$  emission flux in several (typically four) equal variable flux bins across the line profile. Each of these light curves was then cross-correlated with the *B*-band photometric light curve using the methods described in Section 3.1. We discuss the details for the six objects below.

#### 4.1. Individual Objects

**SBS 1116+583A.** While the rms spectrum of this object is rather noisy, there is a clear signature of H $\beta$  variability. The H $\beta$  line was divided up into four velocity bins, two on the blueshifted side and two on the redshifted side, with each bin containing  $\sim 1/4$  the variable H $\beta$  flux. Figure 11 shows the average lag

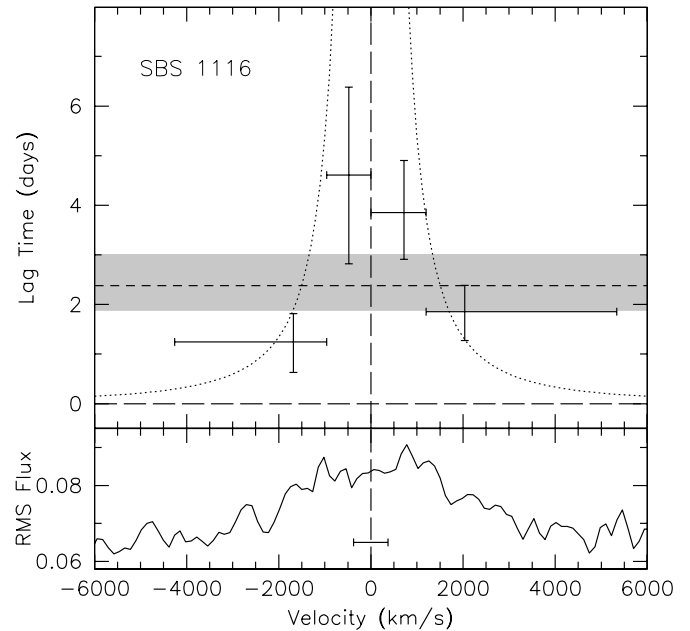


**Figure 11.** Velocity-resolved time lag response (top panel) within the variable broad H $\beta$  emission (bottom panel) in SBS 1116+583A. In the top panel, the vertical error bars show the  $1\sigma$  uncertainties on the time lag within each velocity bin denoted by the horizontal error bars. The horizontal dashed line and gray band mark the average time lag and the  $1\sigma$  uncertainty, respectively, for the entire emission line as listed in Table 9. The dotted curves show the Keplerian envelope for the adopted virial product (as listed in Table 13. In the bottom panel, the horizontal error bar shows the FWHM dispersion determined in Section 3.2.

time for each of these bins as a function of bin velocity relative to the line center. The lag times in the wings of the emission line are not consistent with the measured lag time in the line core, and the profile shows a distinct, symmetric pattern around the line center, as would be expected from a simple model of BLR gas in circular orbits.

**Arp 151.** A similar analysis for Arp 151 was published in Paper I, and here we have updated the analysis to include the slight changes in the data processing. The result is that Figure 12 is not significantly different from Figure 4 of Paper I, and the lag time as a function of velocity in the BLR of Arp 151 shows a significantly asymmetric profile, with longer lags in the blueshifted gas, and shorter lags in the redshifted gas. This pattern is consistent with the expectations from a simple gravitational infall model.

**Mrk 1310.** In the case of Mrk 1310, Figure 13 is rather ambiguous. There is a hint of slightly longer lag times in the line core; however, all of the lags measured in the four velocity bins are consistent with a single value, within the errors. This particular structure is likely consistent with circularly orbiting gas, as there does not seem to be any evidence for a strong redward or blueward asymmetry that would imply radial motion.

**NGC 4748.** Examination of Figure 14 shows that there could be evidence for an outflow in the BLR of NGC 4748. The extremely broad shape of the CCFs for the H $\beta$  flux in this object (see Figure 1) combined with the relatively low-level flux variations results in rather large uncertainties for the measured lag times in this object. Each of the four velocity bins has a lag time that is consistent within  $\sim 1.5\sigma$  of the lag times measured for the other bins, and so the significance of the velocity-resolved structure for NGC 4748 is not clear.

**NGC 5548.** The current low-luminosity state of NGC 5548 has resulted in a very low, broad H $\beta$  line profile which extends



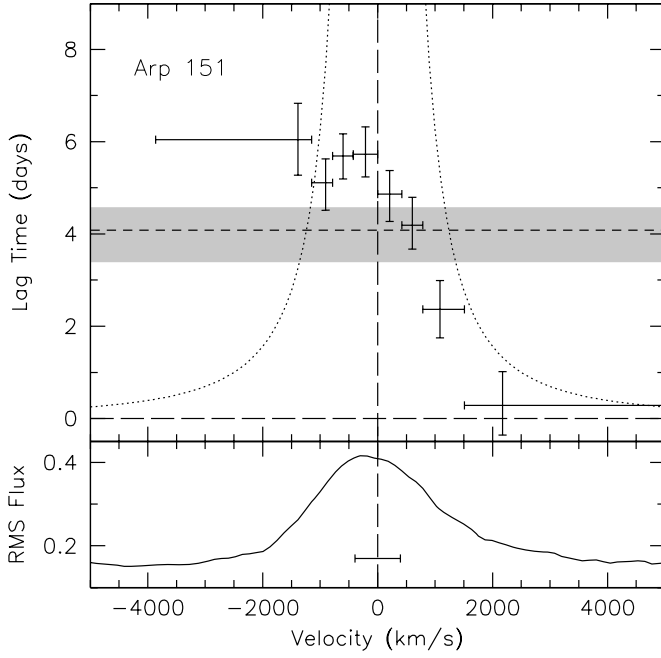


Figure 12. Same as Figure 11 for Arp 151.

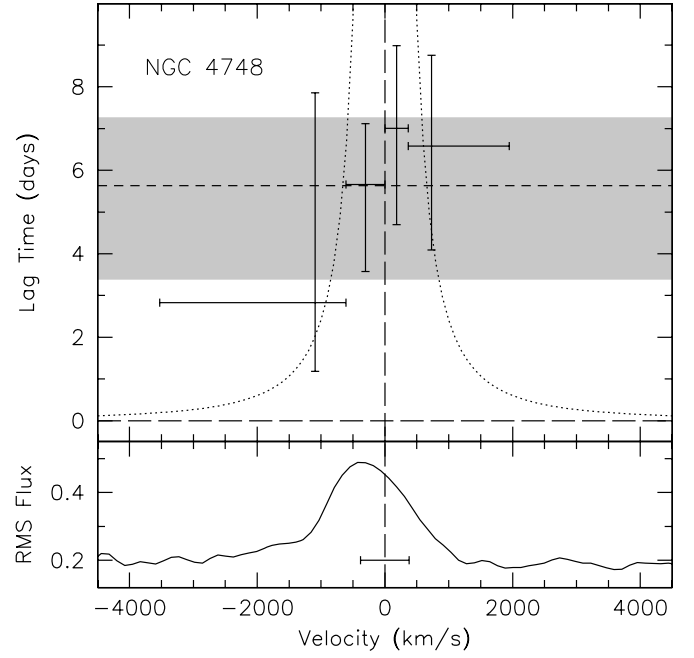


Figure 14. Same as Figure 11 for NGC 4748.

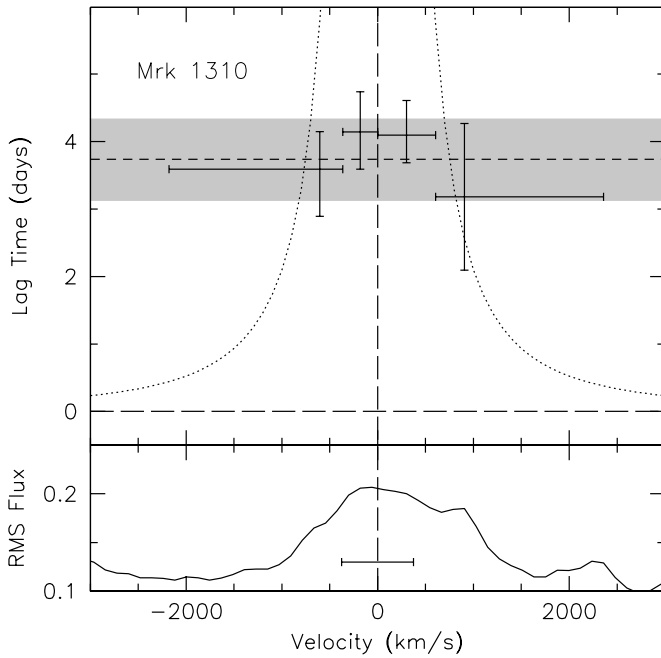


Figure 13. Same as Figure 11 for Mrk 1310.

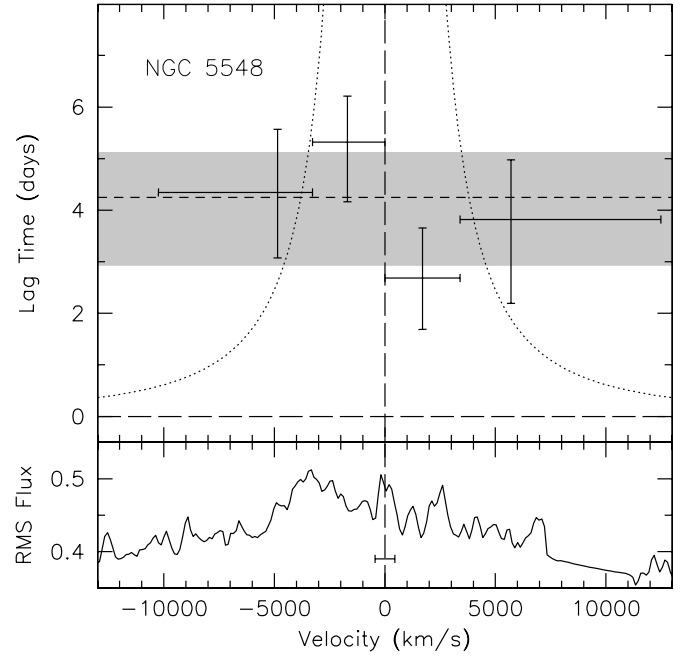


Figure 15. Same as Figure 11 for NGC 5548.

under the [O III] doublet. As the [O III] lines in this object are quite strong, we attempted to subtract them from each spectrum using a very localized linear continuum (which actually includes the red wing of the H $\beta$  profile) before creating the light curves for the four velocity bins. Only the most redward velocity bin is affected by the [O III] lines, and so the measured lag time for that bin may be somewhat suspect. The average lag time for each bin is shown in Figure 15, where there does not seem to be an ordered behavior. In this object as well, each of the measured lag times is generally consistent with the others within the errors, rendering interpretation as somewhat ambiguous.

**NGC 6814.** The lag structure for NGC 6814 as a function of velocity is shown in Figure 16, which again demonstrates that

the lag time measured for each velocity bin is consistent with a constant value, although there is a slight preference for longer lag times in the line core than the wings. This behavior is most likely consistent with gas in circular orbits.

#### 4.2. Discussion

Although several of the objects examined here and presented in Figures 11–16 show somewhat ambiguous or flat time lag behavior as a function of velocity, both SBS 1116 and Arp 151 seem to show clear, and yet completely different, behaviors. The H $\beta$  response in SBS 1116 seems to be consistent with simple, circularly orbiting gas, while gravitational infall seems to be the simplest picture for the H $\beta$  response in Arp 151. The different

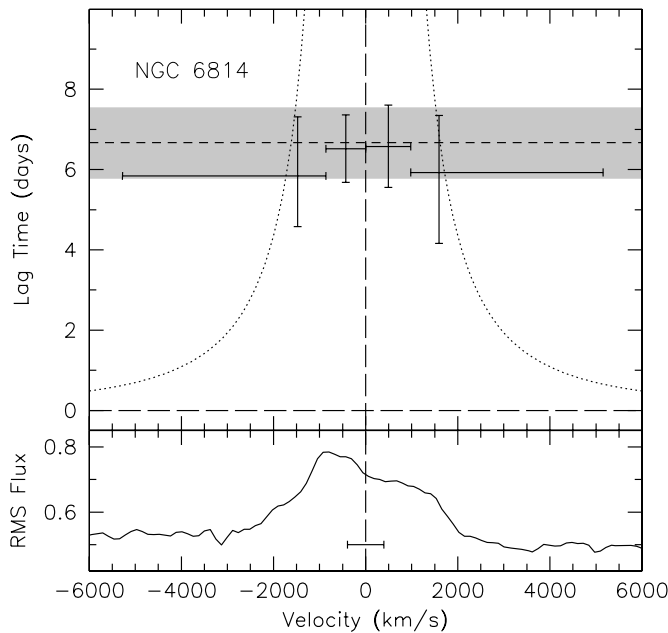


Figure 16. Same as Figure 11 for NGC 6814.

behaviors of lag time as a function of velocity for these two objects may be a clue that BLR structure is very diverse from one object to another, even possibly an evolutionary effect. As such, SBS 1116 and Arp 151 are two excellent targets for further and more detailed analysis using the MEM or other techniques listed above.

While we plan to pursue recovery of full transfer functions for SBS 1116 and Arp 151, we also plan to further examine the situation for the other objects in our sample and determine whether the perceived ambiguity in the velocity-resolved behavior is real or merely a product of the simple analysis employed here. Inspection of the mean time lags in Figure 10(a) shows that the longer lags in the emission-line core differ from the shorter lags in the wings by only  $\sim 1\sigma$ – $2\sigma$ . The addition of typical observational noise to this model could conceivably alter the simplified behavior in Figure 10(a) so that the red crosses are all consistent with a single value, exactly as is seen for several of the objects here such as Mrk 1310 and NGC 6814.

Recovery of a velocity-resolved transfer function for any of these objects could place stringent limits on the  $f$  factor in the determination of the black hole mass for that particular object. There is no reason to expect that the  $f$  value is the same from object to object, and differing  $f$  values in individual objects may be the main source of scatter in the AGN  $M_{\text{BH}}-\sigma_*$  relationship (e.g., Collin et al. 2006). The  $\langle f \rangle$  of 5.5 employed in Section 3.3 is empirically determined and does not assume any specific details of the BLR geometry or kinematics, other than the dominance of the black hole’s gravity. As this population average value has been shown to remove any bias in the sample of reverberation masses when compared to dynamical masses in quiescent galaxies, it is still appropriate to use at this time, even though an individual object’s  $f$  factor may differ. We hope that further analysis of the velocity-resolved information in the LAMP objects may begin to set constraints on the  $f$  factor for individual objects.

## 5. SUMMARY

We have presented the  $H\beta$  emission-line light curves and reverberation analysis for the 13 AGNs included in the LAMP

sample. We measure  $H\beta$  time lags relative to variations in the continuum flux, which are related to the average sizes of the  $H\beta$  BLRs; and we derive black hole masses for the nine objects which display significant time lag signatures. In addition, we also explore the velocity-resolved time lag behavior in six objects and find that the BLR in SBS 1116 seems to be consistent with a simple model of BLR gas in circular orbits, while the BLR in Arp 151 seems to be consistent with gravitationally infalling gas. More work is necessary to determine what constraints may be set on the physical parameters of the BLR in these two objects, as well as whether any constraints may be set for other objects in the sample, although it seems clear that BLR parameters may be very diverse among Type 1 AGNs.

Strong reverberation signals are also seen in other broad emission lines for the objects in this sample, including  $H\alpha$ ,  $H\gamma$ , and  $\text{He II}$ , and future work will focus on the reverberation signals in these emission lines. We have a (*HST*) Cycle 17 program (GO-11662, PI: Bentz) to image the host galaxies of the AGNs in the LAMP sample, which will allow correction for the host-galaxy starlight contribution to the continuum luminosity for each object, and will allow us to extend the low-luminosity end of the  $H\beta$   $R_{\text{BLR}}-L$  relationship, as well as the AGN  $M_{\text{BH}}-L_{\text{bulge}}$  relationship. We also have new measurements of the bulge stellar velocity dispersion for most of the objects in this sample, which will allow us to extend the AGN  $M_{\text{BH}}-\sigma_*$  relationship and explore any updates to the population average  $\langle f \rangle$  value in the black hole mass determinations. Finally, near-infrared photometric monitoring data for a subset of the objects in this sample will allow determination of the reverberation response of the dust torus in those objects (e.g., Minezaki et al. 2004; Suganuma et al. 2004).

We thank the anonymous referee for comments that improved the presentation of this paper. We also thank the excellent staff and support personnel at Lick Observatory for their enormous help during our observing run, and Brad Peterson for helpful conversations and the use of his analysis software. We thank Josh Shiode for his observing help. This work was supported by NSF grants AST-0548198 (UC Irvine), AST-0607485 (UC Berkeley), AST-0642621 (UC Santa Barbara), and AST-0507450 (UC Riverside). J.H.W. gratefully acknowledges support provided by NASA through Hubble Fellowship grant HF-51249 awarded by the Space Telescope Science Institute, which is operated by the Association of Universities for Research in Astronomy, Inc., for NASA, under contract NAS 5-26555. The UC Berkeley researchers also gratefully acknowledge the support of both the Sylvia & Jim Katzman Foundation and the TABASGO Foundation for the continued operation of KAIT. The work of D.S. was carried out at the Jet Propulsion Laboratory, California Institute of Technology, under a contract with NASA.

## REFERENCES

- Bentz, M. C., Peterson, B. M., Netzer, H., Pogge, R. W., & Vestergaard, M. 2009a, *ApJ*, **697**, 160
- Bentz, M. C., Peterson, B. M., Pogge, R. W., & Vestergaard, M. 2009b, *ApJ*, **694**, L166
- Bentz, M. C., Peterson, B. M., Pogge, R. W., Vestergaard, M., & Onken, C. A. 2006a, *ApJ*, **644**, 133
- Bentz, M. C., et al. 2006b, *ApJ*, **651**, 775
- Bentz, M. C., et al. 2007, *ApJ*, **662**, 205
- Bentz, M. C., et al. 2008, *ApJ*, **689**, L21 (Paper I)
- Blandford, R. D., & McKee, C. F. 1982, *ApJ*, **255**, 419
- Bottoff, M., Korista, K. T., Shlosman, I., & Blandford, R. D. 1997, *ApJ*, **479**, 200

- Chiang, J., & Murray, N. 1996, [ApJ](#), **466**, 704
- Collin, S., Kawaguchi, T., Peterson, B. M., & Vestergaard, M. 2006, [A&A](#), **456**, 75
- de Grijp, M. H. K., Keel, W. C., Miley, G. K., Goudfrooij, P., & Lub, J. 1992, [A&AS](#), **96**, 389
- Denney, K., et al. 2006, [ApJ](#), **653**, 152
- Denney, K., et al. 2009, [ApJ](#), **702**, 1353
- Done, C., & Krolik, J. H. 1996, [ApJ](#), **463**, 144
- Ferrarese, L., & Merritt, D. 2000, [ApJ](#), **539**, L9
- Filippenko, A. V. 1982, [PASP](#), **94**, 715
- Gaskell, C. M., & Peterson, B. M. 1987, [ApJS](#), **65**, 1
- Gaskell, C. M., & Sparke, L. S. 1986, [ApJ](#), **305**, 175
- Gebhardt, K., et al. 2000, [ApJ](#), **539**, L13
- Greene, J. E., & Ho, L. C. 2007, [ApJ](#), **667**, 131
- Grier, C. J., et al. 2008, [ApJ](#), **688**, 837
- Heckman, T. M. 1976, [PASP](#), **88**, 844
- Horne, K. 1994, in ASP Conf. Ser. 69, Reverberation Mapping of the Broad-Line Region in Active Galactic Nuclei, ed. P. M. Gondhalekar, K. Horne, & B. M. Peterson (San Francisco, CA: ASP), 23
- Horne, K., Peterson, B. M., Collier, S. J., & Netzer, H. 2004, [PASP](#), **116**, 465
- Kaspi, S., Maoz, D., Netzer, H., Peterson, B. M., Vestergaard, M., & Jannuzi, B. T. 2005, [ApJ](#), **629**, 61
- Kaspi, S., Smith, P. S., Netzer, H., Maoz, D., Jannuzi, B. T., & Giveon, U. 2000, [ApJ](#), **533**, 631
- Kollatschny, W. 2003, [A&A](#), **407**, 461
- Koratkar, A. P., & Gaskell, C. M. 1991, [ApJ](#), **370**, L61
- Krolik, J. H., & Done, C. 1995, [ApJ](#), **440**, 166
- Landolt, A. U. 1992, [AJ](#), **104**, 340
- Laor, A. 1998, [ApJ](#), **505**, L83
- Magorrian, J., et al. 1998, [AJ](#), **115**, 2285
- Marconi, A., & Hunt, L. K. 2003, [ApJ](#), **589**, L21
- Marziani, P., Sulentic, J. W., Zamanov, R., Calvani, M., Dultzin-Hacyan, D., Bachev, R., & Zwitter, T. 2003, [ApJS](#), **145**, 199
- Matthews, T. A., & Sandage, A. R. 1963, [ApJ](#), **138**, 30
- McGill, K. L., Woo, J.-H., Treu, T., & Malkan, M. A. 2008, [ApJ](#), **673**, 703
- McLure, R. J., & Jarvis, M. J. 2002, [MNRAS](#), **337**, 109
- Minezaki, T., Yoshii, Y., Kobayashi, Y., Enya, K., Suganuma, M., Tomita, H., Aoki, T., & Peterson, B. A. 2004, [ApJ](#), **600**, L35
- Morris, S. L., & Ward, M. J. 1988, [MNRAS](#), **230**, 639
- Netzer, H. 1990, in Active Galactic Nuclei, ed. R. D. Blandford et al. (Berlin: Springer), 57
- Onken, C. A., Ferrarese, L., Merritt, D., Peterson, B. M., Pogge, R. W., Vestergaard, M., & Wandel, A. 2004, [ApJ](#), **615**, 645
- Onken, C. A., & Peterson, B. M. 2002, [ApJ](#), **572**, 746
- Peterson, B. M. 1993, [PASP](#), **105**, 247
- Peterson, B. M. 2001, in Advanced Lectures on the Starburst-AGN, ed. I. Aretxaga, D. Kunth, & R. Mújica (Singapore: World Scientific), 3
- Peterson, B. M., & Wandel, A. 1999, [ApJ](#), **521**, L95
- Peterson, B. M., Wanders, I., Bertram, R., Hunley, J. F., Pogge, R. W., & Wagner, R. M. 1998a, [ApJ](#), **501**, 82
- Peterson, B. M., Wanders, I., Horne, K., Collier, S., Alexander, T., Kaspi, S., & Maoz, D. 1998b, [PASP](#), **110**, 660
- Peterson, B. M., et al. 1991, [ApJ](#), **368**, 119
- Peterson, B. M., et al. 2000, [ApJ](#), **542**, 161
- Peterson, B. M., et al. 2002, [ApJ](#), **581**, 197
- Peterson, B. M., et al. 2004, [ApJ](#), **613**, 682
- Peterson, B. M., et al. 2005, [ApJ](#), **632**, 799
- Pijpers, F. P., & Wanders, I. 1994, [MNRAS](#), **271**, 183
- Salpeter, E. E. 1964, [ApJ](#), **140**, 796
- Schlegel, D. J., Finkbeiner, D. P., & Davis, M. 1998, [ApJ](#), **500**, 525
- Schmitt, H. R., Donley, J. L., Antonucci, R. R. J., Hutchings, J. B., & Kinney, A. L. 2003, [ApJS](#), **148**, 327
- Sekiguchi, K., & Menzies, J. W. 1990, [MNRAS](#), **245**, 66
- Smith, H. J., & Hoffleit, D. 1963, [Nature](#), **198**, 650
- Storey, P. J., & Zeppen, C. J. 2000, [MNRAS](#), **312**, 813
- Suganuma, M., et al. 2004, [ApJ](#), **612**, L113
- Tremaine, S., et al. 2002, [ApJ](#), **574**, 740
- Ulrich, M.-H., & Horne, K. 1996, [MNRAS](#), **283**, 748
- van den Bergh, S., Herbst, E., & Pritchett, C. 1973, [AJ](#), **78**, 375
- van Groningen, E., & Wanders, I. 1992, [PASP](#), **104**, 700
- Véron, P., & Hawkins, M. R. S. 1995, [A&A](#), **296**, 665
- Vestergaard, M., & Peterson, B. M. 2006, [ApJ](#), **641**, 689
- Walsh, J. L., et al. 2009, [ApJS](#), in press (Paper II)
- Wandel, A., Peterson, B. M., & Malkan, M. A. 1999, [ApJ](#), **526**, 579
- Wanders, I., et al. 1995, [ApJ](#), **453**, L87
- Weedman, D. W. 1972, [ApJ](#), **171**, 5
- Welsh, W. F., & Horne, K. 1991, [ApJ](#), **379**, 586
- White, R. J., & Peterson, B. M. 1994, [PASP](#), **106**, 879
- Whittle, M. 1992, [ApJS](#), **79**, 49
- Yee, H. K. C. 1980, [ApJ](#), **241**, 894
- Yoshii, Y. 2002, in New Trends in Theoretical and Observational Cosmology ed. K. Sato & T. Shiromizu (Tokyo: Universal Academy), 235
- Yoshii, Y., Kobayashi, Y., & Minezaki, T. 2003, [BAAS](#), **202**, 3803
- Zel'dovich, Y. B., & Novikov, I. D. 1964, [Sov. Phys. Doklady](#), **9**, 246